Exploring the supersymmetric $U(1)_{B-L} \times U(1)_R$ model with dark matter, muon $g-2$, and Z' mass limits

Mariana Frank* and Özer Özdal†

Department of Physics, Concordia University, 7141 Sherbrooke St. West, Montreal, Quebec H4B 1R6, Canada

(Received 20 September 2017; published 25 January 2018)

We study the low scale predictions of the supersymmetric standard model extended by $U(1)_{B-L} \times U(1)_R$ symmetry, obtained from $SO(10)$ breaking via a left-right supersymmetric model, imposing universal boundary conditions. Two singlet Higgs fields are responsible for the radiative $U(1)_{B-L} \times U(1)_R$ symmetry breaking, and a singlet fermion S is introduced to generate neutrino masses through an inverse seesaw mechanism. The lightest neutralino or sneutrino emerge as dark matter candidates, with different low scale implications. We find that the composition of the neutralino lightest supersymmetric particle (LSP) changes considerably depending on the neutralino LSP mass, from roughly half $U(1)_R$ bino, half minimal supersymmetric model (MSSM) bino, to a singlet higgsino, or completely dominated by the MSSM higgsino. The sneutrino LSP is statistically much less likely, and when it occurs it is a 50-50 mixture of right-handed sneutrino and the scalar $\tilde{S}$. Most of the solutions consistent with the relic density constraint survive the XENON 1T exclusion curve for both LSP cases. We compare the two scenarios and investigate parameter space points and find consistency with the muon anomalous magnetic moment only at the edge of a 2σ deviation from the measured value. However, we find that the sneutrino LSP solutions could be ruled out completely by the strict reinforcement of the recent Z' mass bounds. We finally discuss collider prospects for testing the model.

DOI: 10.1103/PhysRevD.97.015012

I. INTRODUCTION

The discovery of the SM-like Higgs boson, while completing the particle content of the Standard Model (SM), has not slowed down the search for new physics. As it stands, the SM may be viable over a certain energy range, but is incomplete, since it fails to explain properties such as the hierarchy problem, neutrino masses, cosmological inflation, and dark matter. As well, a Higgs mass of 125 GeV presents a problem for the SM (e.g., electroweak vacuum instability), and for most of its extensions. Thus constructing and studying viable alternatives, models which aim to solve some of the outstanding problems in SM, are both justified and necessary. Out of these, supersymmetry presents a compelling solution to the hierarchy problem and a clear one for dark matter. However, in its minimal incarnation, the minimal supersymmetric model (MSSM), it shares some of its outstanding problems with the SM.

Some of these issues may be resolved in models with extended gauge groups. In these models, additional D-term contributions to the Higgs mass matrices weaken considerably MSSM mass limits [1–3]. Depending on the models studied, these models can also resolve additional problems of MSSM. For instance, models with left-right symmetry [4] can yield neutrino masses via the seesaw mechanism [5–7].

In [8], an extended supersymmetric model based on $SU(3)_C \times SU(2)_L \times U(1)_R \times U(1)_{B-L}$ was proposed. The model can be embedded in $SO(10)$ SUSY-GUT, much like the left-right supersymmetric model, and generate a new seesaw mechanism for neutrino masses. The factor $U(1)_R$ can be thought off as a remnant of a more complete $SU(2)_R$. Unlike the left-right supersymmetric model, which requires Higgs triplet representations with vacuum expectation values (VEV) $v_R \sim 10^{15}$ GeV for obtaining neutrino masses and gauge unification, the symmetry in this model can be broken by singlet Higgs bosons (thought of as remnants of a doublet representation in left-right models), with VEVs in the TeV range, while still allowing for gauge coupling unification. In [8], the smallness of neutrino masses was explained as based on an inverse

*mariana.frank@concordia.ca
†ozer.ozdal@concordia.ca

seesaw mechanism. The general features of the TeV scale soft-supersymmetry breaking parameters were explored in [9], outlining conditions for models with intermediate scales obtained from breaking $SO(10)$. The Higgs sector of the model was further explored, showing that a larger mass than that predicted by the MSSM can be obtained. The parameter space was further explored in [10], where benchmarks, branching ratios, as well as lepton violation constraints were analyzed.

In this work, we concentrate on investigating, discriminating, and restricting the parameter space of the model using dark matter studies. We include up-to-date constraints on the spectrum coming from the Higgs signal strengths and mass data, and including LHC restrictions on squark and gluino masses, constraints on flavor parameters from the B sector, as well as recent lower limits on the Z' mass. Assuming universal scalar and gaugino masses, we show that the lightest supersymmetric particle (LSP) can be the sneutrino (which is different from the usual in this scenario, being a mixture of the right sneutrino and a gauge singlet fermion introduced to generate the inverse seesaw mechanism); or the lightest neutralino [which is favored to be a mixture of the two $U(1)$ binos]. Relic density and indirect dark matter detection severely restrict the parameter space, as indeed does the recent limit on the Z' mass [11]. Within the parameter space allowed by dark matter limits, we analyze the consequences on sparticle spectra, the neutral Higgs sector and on the anomalous magnetic moment of the muon, which shows more than a 3σ [12] discrepancy with the SM prediction. Finally we investigate the possibilities of testing the model at the LHC.

Our work is organized as follows. We provide a brief description of the model in Sec. II, capitalizing on more complete descriptions which have appeared previously. In Sec. III we describe in detail the parameters of the model and constraints imposed on them. Dark matter phenomenology is explored in Sec. IV, for both neutralino LSP IV A and sneutrino LSP IV B. We then look at the consequences of our findings and compare the two scenarios in Sec. V, for the sparticle spectrum, the Higgs sector V A and the anomalous magnetic moment of the muon V B, and show that imposing the Z' strict mass limits basically rules out the sneutrino DM solutions in V C. We discuss possibilities for detection in Sec. VI and conclude in Sec. VII. We leave some relevant formulas for the Appendix.

II. MODEL DESCRIPTION

In this section, we describe the supersymmetric model under investigation briefly. This model, based on $SU(3)_c \times SU(2)_L \times U(1)_R \times U(1)_{B-L}$ (thereafter referred to as the BLRSSM) was first introduced in [8] and further studied in [9,10,13]. The model emerges from breaking of supersymmetric $SO(10)$ to the SM through the following intermediary steps:

$$\begin{aligned} SO(10) &\to SU(3)_C \times SU(2)_L \times SU(2)_R \times U(1)_{B-L} \\ &\to SU(3)_C \times SU(2)_L \times U(1)_R \times U(1)_{B-L} \\ &\to SU(3)_C \times SU(2)_L \times U(1)_Y. \end{aligned}$$

The advantages of this model are

(i) It is obtained by the breaking of SO(10) through a left-right symmetric model, thus inheriting some of its attractive features [4,14];
(ii) It is able to explain neutrino masses by the inverse seesaw mechanism [8];
(iii) It preserves gauge coupling unification of the MSSM, even when the breaking scale in the last step is of the order of the electroweak scale [9];
(iv) It resolves the MSSM Higgs mass problem by yielding larger Higgs masses through additional D-terms in the soft-breaking potential, without resorting to heavy particles [9];
(v) It could yield signals differentiating it from MSSM, which may lie in different regions of SUSY parameter space;
(vi) It could provide different dark matter candidates and phenomenology, which in turn informs the study of direct and indirect searches.

The particle content of the model contains, in addition to the SM particles:

(1) In the fermionic/matter sector, an additional (right-handed) neutrino N_i^c, required for anomaly cancellation, and an additional singlet fermion S, needed for generating neutrino masses. Both these fermions come in three families and are accompanied by their scalar partners;
(2) In the bosonic/Higgs sector, two new Higgs fields, $\mathcal{X}_R$ and $\overline{\mathcal{X}}_R$, remnants of $SU(2)_R$ doublets, needed to break $U(1)_R \times U(1)_{B-L} \to U(1)_Y$, and their fermionic partners;
(3) In the gauge sector, an additional neutral gauge field, Z', which emerges from the mixing of the neutral gauge fields of $SU(2)_L, U(1)_R$ and $U(1)_{B-L}$, (W^0, B_R, B_{B-L}), and its fermionic partner.

In a sense, the model described here is minimal: however it requires an extra $\mathcal{Z}_2$ matter parity to avoid breaking of R-parity [10].

The superpotential in this model is described by

$$\begin{aligned} W = {} & \mu H_u H_d + Y_u^{ij} Q_i H_u u_j^c - Y_d^{ij} Q_i H_d d_j^c - Y_e^{ij} L_i H_d e_j^c \\ & + Y_\nu^{ij} L_i H_u N_i^c + Y_s^{ij} N_i^c \mathcal{X}_R S - \mu_R \bar{\mathcal{X}}_R \mathcal{X}_R + \mu_S S S, \end{aligned} \quad (2.1)$$

where the first line of Eq. (2.1) contains the usual terms of the MSSM, while the second line includes the additional interactions from the right-handed neutrino N_i^c and the singlet Higgs fields $\overline{\mathcal{X}}_R$, $\mathcal{X}_R$ with $-1/2$ and $+1/2$ $B-L$, and $+1/2$ and $-1/2$ R charges, respectively. The first term of the second line in superpotential describes the Yukawa

interactions between neutrinos, and Y_ν^{ij} is the Yukawa coupling associated with these interactions. In a similar manner, Y_s^{ij} represents the Yukawa coupling among N_i^c, $\mathcal{X}_R$ and S. Moreover, μ_R is similar to μ' term of the $B-L$ extension of supersymmetric model (BLSSM) and stands for bilinear mixing between $\mathcal{X}_R$ and $\overline{\mathcal{X}}_R$ fields. Note that there is also a μ_S term to generate nonzero neutrino masses with an inverse seesaw mechanism, and as customary, it is restricted to have a low value, as it cannot give important contributions to any other sector except for neutrinos. Contrary to the BLSSM [15–17], where neutrinos have Majorana mass terms, N_i^c fields interact with $\mathcal{X}_R$ and S through $Y_s^{ij} N_i^c \mathcal{X}_R S$ term, and lead to SM-singlet pseudo-Dirac mass eigenstates. Besides, the interaction of the $SU(2)_L$ singlet Higgs fields $\mathcal{X}_R$, S and N_i^c yield a significant contribution to the masses of the extra Higgs bosons. Implementing the inverse seesaw mechanism into the model allows Y_ν^{ij} and Y_s^{ij} to be at the order of unity. Hence, the contribution from the right-handed neutrino sector to the Higgs boson cannot be neglected and yields a different low scale phenomenology from the MSSM and BLSSM with an inverse seesaw mechanism [18–20].

The soft-breaking Lagrangian terms in the model are

$$
\begin{aligned}
-\mathcal{L}_{SB,W} &= -B_\mu(H_u^0 H_d^0 - H_d^- H_u^+) - B_{\mu_R}\mathcal{X}_R\bar{\mathcal{X}}_R + A_u(\tilde{u}_{R,i}^\star \tilde{u}_{L,j} H_u^0 - \tilde{u}_{R,i}^\star \tilde{d}_{L,j} H_u^+) + A_d(\tilde{d}_{R,i}^\star \tilde{d}_{L,j} H_d^0 - \tilde{d}_{R,i}^\star \tilde{u}_{L,j} H_d^-) \\
&\quad + A_e(\tilde{e}_{R,i}^\star \tilde{e}_{L,j} H_d^0 - \tilde{e}_{R,i}^\star \tilde{\nu}_{L,j} H_d^-) + A_\nu(\tilde{\nu}_{R,i}^\star \tilde{\nu}_{L,j} H_u^0 - \tilde{e}_{R,i}^\star \tilde{\nu}_{L,j} H_u^-) + A_{s,ij}\mathcal{X}_R \tilde{\nu}_{R,i} \tilde{S} + \text{H.c.}, \\
-\mathcal{L}_{SB,\phi} &= m_{\mathcal{X}_R}^2 |\mathcal{X}_R|^2 + m_{\bar{\mathcal{X}}_R}^2 |\bar{\mathcal{X}}_R|^2 + m_{H_d}^2(|H_d^0|^2 + |H_d^-|^2) + m_{H_u}^2(|H_u^0|^2 + |H_u^+|^2) + m_{q,ij}^2(\tilde{d}_{L,i}^\star \tilde{d}_{L,j} + \tilde{u}_{L,i}^\star \tilde{u}_{L,j}) \\
&\quad + m_{d,ij}^2 \tilde{d}_{R,i}^\star \tilde{d}_{R,j} + m_{u,ij}^2 \tilde{u}_{R,i}^\star \tilde{u}_{R,j} + m_{l,ij}^2(\tilde{e}_{L,i}^\star \tilde{e}_{L,j} + \tilde{\nu}_{L,i}^\star \tilde{\nu}_{L,j}) + m_{e,ij}^2 \tilde{e}_{R,i}^\star \tilde{e}_{R,j} + m_{\nu,ij}^2 \tilde{\nu}_{R,i}^\star \tilde{\nu}_{R,j} + m_{s,ij}^2 \tilde{S}_i^\star \tilde{S}_j \\
-\mathcal{L}_{SB,\lambda} &= \frac{1}{2}(M_1 \lambda_B^2 + M_2 \lambda_W^2 + M_3 \lambda_g^2 + 2M_{B_R}\lambda_B \lambda_R + \text{H.c.}),
\end{aligned}
\tag{2.2}
$$

which contain triple scalar interactions, scalar masses and masses for the gauginos of all gauge groups, denoted by λ's.

The $U(1)_R \times U(1)_{B-L}$ symmetry is broken spontaneously to $U(1)_Y$ by the vacuum expectation values (VEVs) of $\mathcal{X}_R$ and $\overline{\mathcal{X}}_R$

$$
\langle \mathcal{X}_R \rangle = \frac{v_{\mathcal{X}_R}}{\sqrt{2}}, \qquad \langle \bar{\mathcal{X}}_R \rangle = \frac{v_{\bar{\mathcal{X}}_R}}{\sqrt{2}}, \tag{2.3}
$$

while $SU(2)_L \times U(1)_Y$ is broken further to $U(1)_{\text{EM}}$ by the VEVs of the Higgs doublets

$$
\langle H_d^0 \rangle = \frac{v_d}{\sqrt{2}}, \qquad \langle H_u^0 \rangle = \frac{v_u}{\sqrt{2}}. \tag{2.4}
$$

We denote $v_R^2 = v_{\mathcal{X}_R}^2 + v_{\bar{\mathcal{X}}_R}^2$ and $\tan\beta_R = \frac{v_{\mathcal{X}_R}}{v_{\bar{\mathcal{X}}_R}}$, in analogy with $v^2 = v_d^2 + v_u^2$, $\tan\beta = \frac{v_u}{v_d}$. The spectrum for this model, including particle masses, neutrino seesaw, mixing of gauge bosons and the neutralino sector has been discussed before [13], and we do not repeat it here. In what follows we concentrate on scanning the model parameters first by imposing Higgs sector, particle masses and other low energy restrictions, and then looking for dark matter candidates and resolution of the anomalous magnetic moment of the muon, thus restricting the parameter space to region where these conditions are satisfied.

III. SCANNING PROCEDURE AND EXPERIMENTAL CONSTRAINTS

We proceed to analyze the model by scanning the fundamental parameter space of the BLRSSM. We use the SPheno 3.3.3 package [21,22] obtained from the model implementation in Sarah 4.6.0 [23,24]. This package employs renormalization group equations (RGEs), modified by the inverse seesaw mechanism to evolve Yukawa and gauge couplings from M_{GUT} to the weak scale, where M_{GUT} is determined by the requirement of gauge coupling unification. We do not strictly enforce the solutions to unify at M_{GUT}, since a few percent deviation is allowed due to unknown GUT-scale threshold corrections [25]. M_{GUT} is thus dynamically determined by the requirement of gauge unification, that is $g_L = g_R = g_{B-L} \approx g_3$, with subindices denoting the gauge couplings associated with $SU(2)_L$, $SU(2)_R$, $U(1)_{B-L}$ and $SU(3)_C$ respectively. With boundary conditions determined at M_{GUT}, all the soft supersymmetry breaking (SSB) parameters along with the gauge and Yukawa couplings are evolved to the weak scale.

We performed random scans over the parameter space, as illustrated in Table I, imposing universal boundary conditions for scalar and gaugino masses. We comment briefly first on the parameters chosen, and then on the constraints

TABLE I. Scanned parameter space.

Parameter	Scanned range	Parameter	Scanned range
m_0	[0., 3.] TeV	v_R	[6.5,20.] TeV
$M_{1/2}$	[0., 3.] TeV	$\text{diag}(Y_\nu^{ij})$	[0.001, 0.99]
A_0/m_0	[−3., 3.]	$\text{diag}(Y_s^{ij})$	[0.001, 0.99]
$\tan\beta$	[0., 60.]	sign of μ	positive
$\tan\beta_R$	[1., 1.2]	sign of μ_R	positive or negative

TABLE II. Current experimental bounds imposed on the scan for consistent solutions.

Observable	Constraints	Reference	Observable	Constraints	Reference
m_{h_1}	[122, 128] GeV	[41]	$m_{\tilde{t}_1}$	≥730 GeV	[42]
$m_{\tilde{g}}$	>1.75 TeV	[42]	$m_{\chi_1^\pm}$	≥103.5 GeV	[42]
$m_{\tilde{\tau}_1}$	≥105 GeV	[42]	$m_{\tilde{b}_1}$	≥222 GeV	[42]
$m_{\tilde{q}}$	≥1400 GeV	[42]	$m_{\tilde{\tau}_1}$	>81 GeV	[42]
$m_{\tilde{e}_1}$	>107 GeV	[42]	$m_{\tilde{\mu}_1}$	>94 GeV	[42]
$\chi^2(\hat{\mu})$	≤2.3	⋯	$\mathrm{BR}(B_s^0 \to \mu^+\mu^-)$	$[1.1, 6.4] \times 10^{-9}$	[35]
$\frac{\mathrm{BR}(B\to\tau\nu_\tau)}{\mathrm{BR}_{\mathrm{SM}}(B\to\tau\nu_\tau)}$	[0.15, 2.41]	[37]	$\mathrm{BR}(B^0 \to X_s\gamma)$	$[2.99, 3.87] \times 10^{-4}$	[36]
$m_{Z'}$	>3.5 TeV	[11]	$\Omega_{\mathrm{DM}}h^2$	[0.09–0.14]	[39,40]

included. Here m_0 corresponds the mass terms for all scalars, and $M_{1/2}$ represents the mass terms for all gauginos, including the ones associated with the $U(1)_{B-L}$ and $U(1)_R$ gauge groups. In setting the ranges for the free parameters, we scan scalar and gaugino SSB mass terms between 0–3 TeV, regions which yield sparticle masses at the low scale, especially the LSP.

Here A_0 is the trilinear scalar interaction coupling coefficient, and we adjusted its range to avoid charge and/or color breaking minima, which translates into $|A_0| \lesssim 3m_0$ [26,27]. Also, $\tan\beta$ is the ratio of vacuum expectation values of the MSSM Higgs doublets v_u/v_d, while $\tan\beta_R$ which denotes the ratio of vacuum expectation values of $v_{\chi_R}/v_{\bar{\chi}_R}$, is also a free parameter in this model. Practically however, $\tan\beta_R$ is required to be close to 1, in order to prevent large D-term contributions to the sfermion masses and to avoid tachyonic solutions. The VEV v_R represents the vacuum expectation value which breaks the extra $U(1)_{B-L} \times U(1)_R$ symmetry. Since the breaking scale of the extra symmetry plays a crucial role in determining the Z' mass, the gauge boson associated with $U(1)_{B-L} \times U(1)_R$ symmetry, we scan v_R between 6.5 and 20 TeV to obtain Z' boson masses consistent with the current experimental bounds.

The parameter μ is the bilinear mixing of the MSSM doublet Higgs fields, while μ_R is the bilinear mixing of the $SU(2)_R$ remnants Higgs fields, which are singlet under $SU(2)_L$ symmetry. The values of μ and μ_R can be determined by the radiative electroweak symmetry breaking (REWSB) but their signs cannot; thus, only their signs remain as free parameters. Since the model contributions to the muon anomalous magnetic moment are related to the sign of $\mu M_{1/2}$, we scan over positive μ values, but we accept both negative and positive solutions of μ_R, while requiring solutions consistent with experimental predictions, and favoring solutions which improve upon the SM predictions for the muon $g-2$ factor. The superpotential of the model also includes a μ_S parameter, which yields nonzero neutrino masses via the inverse seesaw mechanism. However, μ_S is constrained to be small, so that it cannot effect any supersymmetric particle masses or decays. We also fixed the top quark mass to its central value ($m_t = 173.3$ GeV) [28] in our scan. The Higgs boson mass is very sensitive to the top quark mass, and small changes in its value can shift the Higgs boson mass by 1–2 GeV [29,30], although it does not significantly affect sparticle masses [31]. Hence, we scan both $\mathrm{diag}(Y_\nu^{ij})$ and $\mathrm{diag}(Y_s^{ij})$ between 0.001–0.99, though the inverse seesaw mechanism prefers values of an order 1.

In scanning the parameter space, we use the interface which employs the Metropolis-Hasting algorithm described in [32]. All collected data points satisfy the requirement of REWSB. After collecting the data, we impose current experimental mass bounds on all the sparticles and the SM-like Higgs boson as highlighted in Table II. Although we restrict the SM-like Higgs boson to lie between 122–128 GeV with a 3 GeV uncertainty, we also employed the HiggsBounds 4.3.1 package [33] to compare our Higgs sector predictions with the experimental cross section limits from the LHC, and we require agreement with the Higgs boson decay signal strengths at the tree level, $h \to WW^\star$, $h \to ZZ^\star$ and $h \to b\bar{b}$. Thus using the mass-centered χ^2, and selecting the parametrization for the Higgs mass uncertainty as a "box" we employed HiggsSignals 1.4.0 package [34] and bounded the solutions which yield total $\chi^2(\hat{\mu}) \leq 2.3$. Another constraint comes from rare B-decay processes, $B_s \to \mu^+\mu^-$ [35], $b \to s\gamma$ [36] and $B_u \to \tau\nu_\tau$ [37]. The B-meson decay into a muon pairs, in particular, constrains the parameter space since there the SM predictions are consistent with the experimental measurements. The supersymmetric contributions are proportional to $(\tan\beta)^6/m_{A_i}^4$ and constrained to be small. Hence, m_{A_i} has to be heavy enough ($m_{A_i} \sim$ TeV) to suppress the supersymmetric contributions for large $\tan\beta$ values. In addition to these limitations, dark matter observations severely restrict the parameter space, requiring the LSP to be stable and electric and color neutral, which excludes a significant portion of the parameter space where stau is the LSP. We concentrate on two different data sets, one with the neutralino being the LSP, and one where sneutrino is the LSP, and we shall distinguish these two scenarios throughout our investigations. We employ the micrOMEGAs 4.3.1 package [38] and tag the

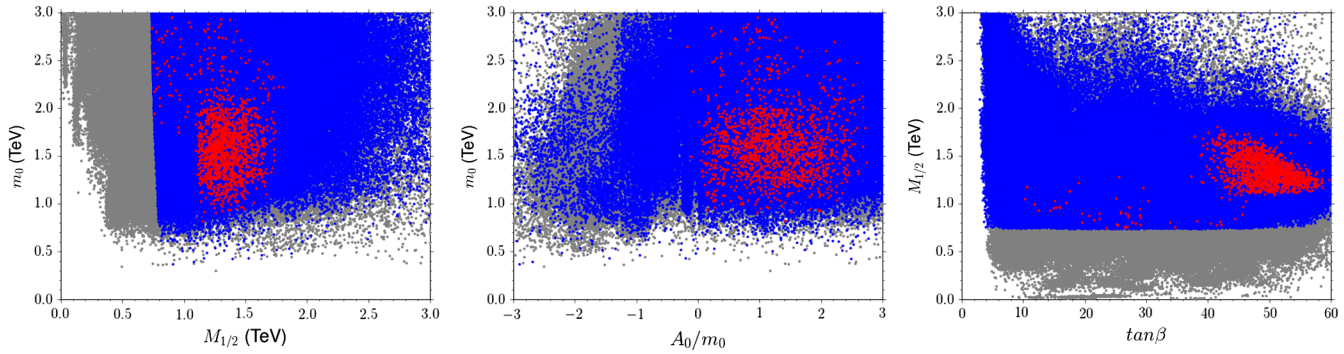

FIG. 1. Parameter scans for the neutralino LSP scenario. (Left) m_0 versus $M_{1/2}$, (center) m_0 versus A_0/m_0 and (right) $M_{1/2}$ versus $\tan\beta$. All points are consistent with REWSB and neutralino LSP. Blue points satisfy all the experimental limits listed in Table II. Red points form a subset of blue and represent solutions consistent with the relic density constraint.

solutions which yield a consistent relic density within the 20% uncertainty range provided from the WMAP data [39,40] as specified in Table II. Apart from a relic abundance constraint, we do not impose any restriction from the dark matter experiments. All the experimental restrictions mentioned above are listed in Table II.

IV. DARK MATTER PHENOMENOLOGY

For either a neutralino or sneutrino to be viable candidates for dark matter, they must yield the correct level of the relic abundance for thermal dark matter production in the early Universe, determined very precisely as the amount of nonbaryonic dark matter in the energy-matter of the Universe, $\Omega_{\rm DM}h^2 = 0.1199 \pm 0.0027$ [43], with $\Omega_{\rm DM}$ being the energy density of the dark matter with respect to the critical energy density of the Universe, and h the reduced Hubble parameter.

In addition, as the lack of any dark matter signals in either direct or indirect dark matter detection experiments confront our theoretical expectations, these must satisfy increasingly severe constraints from experiments. The interaction of dark matter with a detector nuclear matter can be spin-dependent or spin-independent. The spin-dependent scattering can only happen for odd-numbered nucleons in the nucleus of the detector material, while in spin-independent (scalar) scattering, the coherent scattering of all the nucleons in the nucleus with the DM are added in phase. Consequently, in direct detection experiments, the experimental sensitivity to spin-independent (SI) scattering is much larger than the sensitivity to spin-dependent scattering, and thus we shall concentrate on the former.

We proceed as follows. First, we analyze the consequences of having the lightest neutralino as the dark matter candidate. Using the results in the previous sections, we explore the parameter space of the model which is consistent with this assumption. We follow in the next section with the parameter restrictions for the sneutrino dark matter.

A. Neutralino dark matter

In this section, we concentrate on analyzing the consequences on the mass spectrum of the BLRSSM obtained by scanning over the parameter space given in Table I where the lightest neutralino ($\tilde{\chi}_1^0$) is always the LSP and highlight the solutions compatible with the constraints showed in Table II. We start with Fig. 1 which displays the allowed parameter regions, with plots in $m_0 - M_{1/2}$, $m_0 - A_0/m_0$ and $M_{1/2} - \tan\beta$ planes. Throughout the graphs, all points satisfy REWSB. Blue points satisfy all experimental mass bounds, signal strengths of the SM-like Higgs boson and rare B-decay constraints given in Table II. Red points obey the above mentioned constraints, as well as the relic density bounds, $0.09 \leq \Omega_{\rm DM}h^2 \leq 0.14$. The $m_0 - M_{1/2}$ plane shows that solutions for $M_{1/2} \lesssim 800$ GeV are excluded by the constraints in Table II, and the requirement of a consistent relic density (red points) excludes a significant portion of the LHC allowed region (blue points). For $M_{1/2} \sim 1$ TeV, m_0 is bounded between 2–3 TeV, and low m_0 values can survive for larger $M_{1/2}$. On the other hand, the $m_0 - A_0/m_0$ panel shows that the regions with larger m_0 values prefer positive values of the trilinear scalar interaction strength A_0, while almost all solutions with a consistent relic density have a positive A_0 parameter. Unlike the $B - L$ Supersymmetric Standard Model (BLSSM) [16], where negative A_0 solutions for $m_0 \geq 1$ TeV do not satisfy the REWSB, here all LSP constraints can be fulfilled for this portion of the parameter space, while only the relic density constraint imposes positivity of A_0. The $M_{1/2} - \tan\beta$ plot indicates that it is possible to find solutions with $0.09 \leq \Omega_{\rm DM}h^2 \leq 0.14$ only for large $\tan\beta$ values, $40 \leq \tan\beta \leq 60$, although it is easier to satisfy LHC limitations for low $\tan\beta$ values.

In Fig. 2, we show specific results for the determination of a sparticle mass spectrum, with plots in (top left) $m_{\tilde{t}_1} - m_{\tilde{\chi}_1^0}$, (top right) $m_{\tilde{b}_1} - m_{\tilde{\chi}_1^0}$, (bottom left) $m_{\tilde{\chi}_1^\pm} - m_{\tilde{\chi}_1^0}$ and (bottom right) $m_{\tilde{\tau}_1} - m_{\tilde{\chi}_1^0}$ planes. The color coding is the same as Fig. 1. Furthermore, the mass region in which

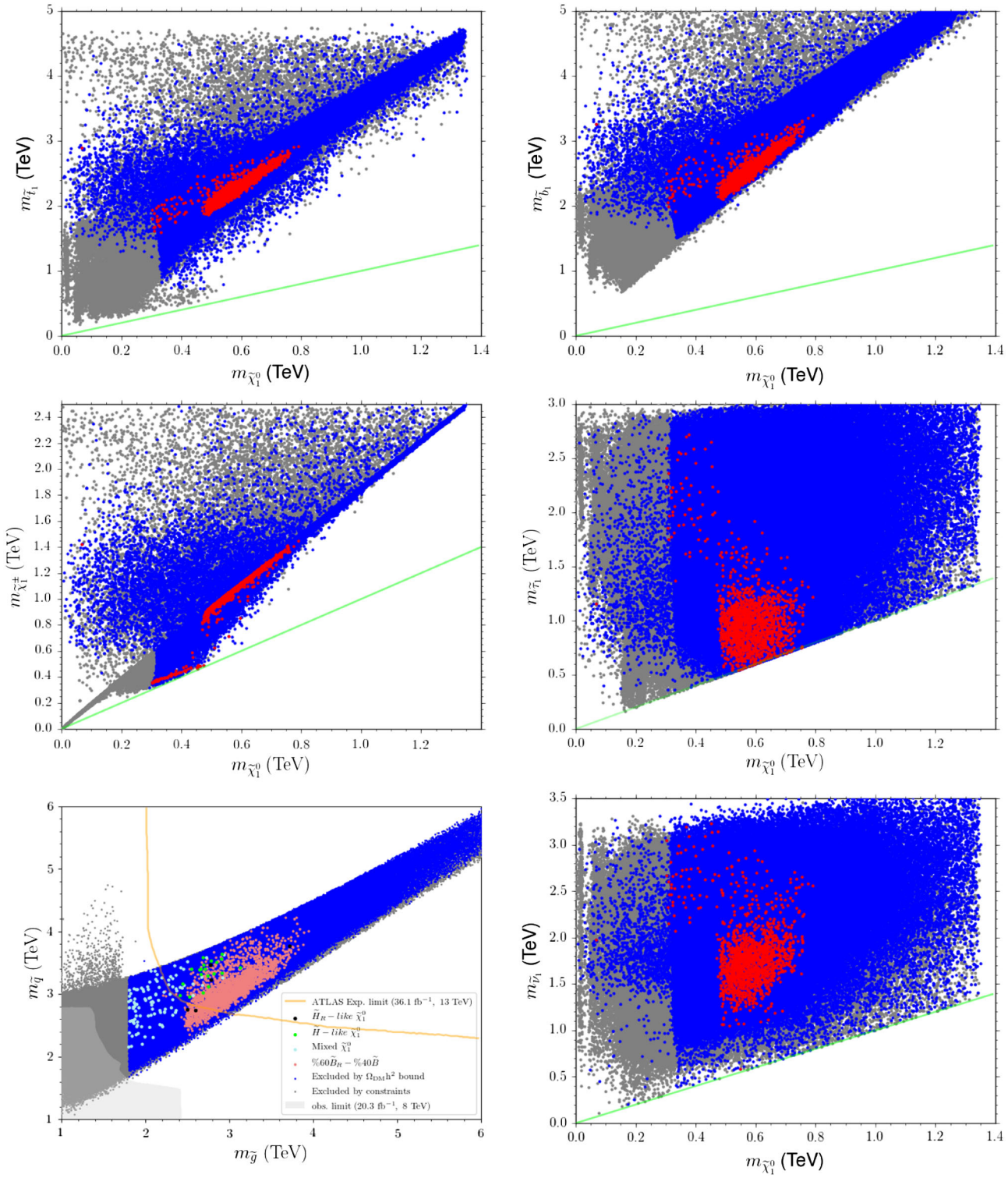

FIG. 2. Plots in (top left) $m_{\tilde{t}_1} - m_{\tilde{\chi}_1^0}$, (top right) $m_{\tilde{b}_1} - m_{\tilde{\chi}_1^0}$, (middle left) $m_{\tilde{\chi}_1^\pm} - m_{\tilde{\chi}_1^0}$, (middle right) $m_{\tilde{\tau}_1} - m_{\tilde{\chi}_1^0}$, (bottom left) $m_{\tilde{q}} - m_{\tilde{g}}$, and (bottom right) $m_{\tilde{\nu}_1} - m_{\tilde{\chi}_1^0}$ planes. The color coding is the same as Fig. 1. In the bottom left panel, the color coding represents the neutralino composition as indicated in the inset. The solid line in each plane indicates the degenerate mass region.

the two masses are degenerate is displayed as a solid green line. We note that the LSP neutralino solutions consistent with the relic density bound can be obtained only when 300 GeV $\leq m_{\tilde{\chi}_1^0} \leq$ 800 GeV. As can be seen from $m_{\tilde{t}_1} - m_{\tilde{\chi}_1^0}$ and $m_{\tilde{b}_1} - m_{\tilde{\chi}_1^0}$ planes, we find that stop and sbottom masses have to be at least ~1.5 TeV and 2 TeV respectively to fulfill all the restrictions. Even though it is possible to find light stop solutions ($m_{\tilde{t}_1} \leq 1$ TeV) when

340 GeV $\leq m_{\tilde{\chi}_1^0} \leq$ 550 GeV, the relic density condition is not satisfied for these solutions. Moreover, unlike the results of BLSSM [16] where the lightest chargino masses are always above 600 GeV, here the $m_{\tilde{\chi}_1^\pm} - m_{\tilde{\chi}_1^0}$ plot shows that there is a region of parameter space where the lightest chargino solutions are nearly degenerate with the lightest neutralino when 300 GeV $\leq m_{\tilde{\chi}_1^0} \leq$ 500 GeV. These solutions correspond to the case where the lightest chargino decays into the neutralino LSP and $W/W^\star$ boson ($\tilde{\chi}_1^\pm \to \tilde{\chi}_1^0 + W^\pm(W^{\star\pm})$), and the branching ratio for this channel is almost 1. On the bottom right panel, the $m_{\tilde{\tau}_1} - m_{\tilde{\chi}_1^0}$ plane illustrates the stau mass along with the LSP neutralino mass. There is a parameter space around $m_{\tilde{\chi}_1^0} \sim 600$ GeV, where the stau mass is almost degenerate with the LSP neutralino and becomes the next to lightest supersymmetric particle (NLSP), but also for a region of the parameter space, the stau can be much heavier than the neutralino LSP. The lightest stau NLSP solutions compatible with the relic density constraint occur around 500 GeV. One can choose one of these solutions and study relevant neutralino annihilation processes mediated by a light stau [44].

The bottom plots in Fig. 2 show our results for the sparticle spectrum for the gluino and sneutrinos, with the plots in $m_{\tilde{q}} - m_{\tilde{g}}$ (where $\tilde{q}$ represents squarks from the first two families) and $m_{\tilde{\nu}_1} - m_{\tilde{\chi}_1^0}$ planes. The $m_{\tilde{q}} - m_{\tilde{g}}$ plane shows that squarks masses for the first two families and gluino masses should be heavier than 2.2 TeV but lighter than 4 TeV (orange points). Although the relic density condition and the current ATLAS experimental limit [45] strictly constrain the crucial portion of the parameter space, most of the solutions are consistent with this experimental exclusion. Finally, the $m_{\tilde{\nu}_1} - m_{\tilde{\chi}_1^0}$ plane reveals that it is hard to find solutions with a sneutrino as the supersymmetric NLSP if we require consistency with the relic density bound, and the lightest sneutrino solutions satisfying all bounds can be obtained at around 1 TeV.

Note that the graphs contain also information on the composition of the neutralino LSP. As can be seen from the

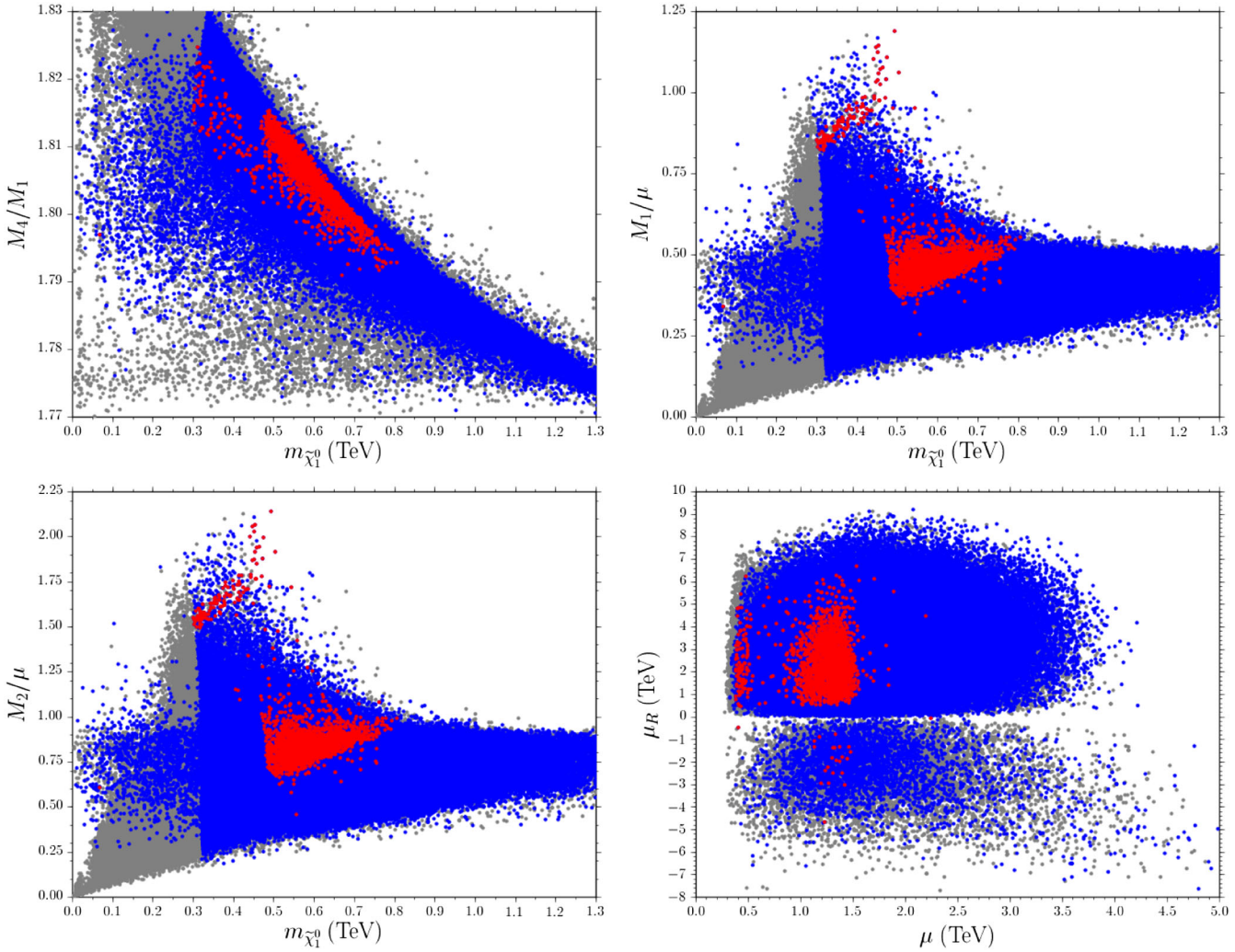

FIG. 3. Plots for the neutralino LSP mass and mass ratios: (top left) M_4/M_1, (top right) M_1/μ, (bottom left) M_2/μ, and (bottom right) μ_R–μ correlations. The color coding is the same as Fig. 1.

gluino versus squarks panel, light blue points, which represent the mixed neutralino LSP solutions consistent with the relic density bounds, are mostly found under the yellow curve (the excluded region). However, orange points representing mixtures of R-bino and $B-L$ bino [gauginos of $U(1)_R$ and $U(1)_{B-L}$, respectively] as well as green and black points which stand for $\tilde{H}$-like and $\tilde{H}_R$-like neutralino LSPs respectively are mostly located within the 1 sigma error of the yellow line.

To continue the investigation of the neutralino LSP composition, in Fig. 3 we plot the correlation between the neutralino mass and gaugino and higgsino mass ratios with (top left) M_4/M_1, (top right) M_1/μ, (bottom left) M_2/μ, and (bottom right) $\mu_R-\mu$, for the correct relic density. The color coding is the same as Fig. 1. According to the $M_4/M_1-m_{\tilde{\chi}_1^0}$ plane, there must be a clear relation between the $B-L$ bino $\tilde{B}$ and $\tilde{B}_R$ masses so that the ratio of $\tilde{B}_R/\tilde{B}$ should be at around $\sim$1.8, decreasing slightly when the neutralino LSP mass increases. The next two plots compare the bino-higgsino (top right) and wino-higgsino (bottom left) masses, respectively, by looking at their mass ratio. In the top right plot, almost all solutions satisfying LHC collider bounds, and *all* solutions satisfying relic density constraints have $M_1/\mu \lesssim 1$, that is the bino is lighter than the higgsino mass parameter. The left bottom plane shows that, despite allowing for light higgsinos, the wino is mostly lighter than the higgsino over all the parameter space where relic density bounds are satisfied.

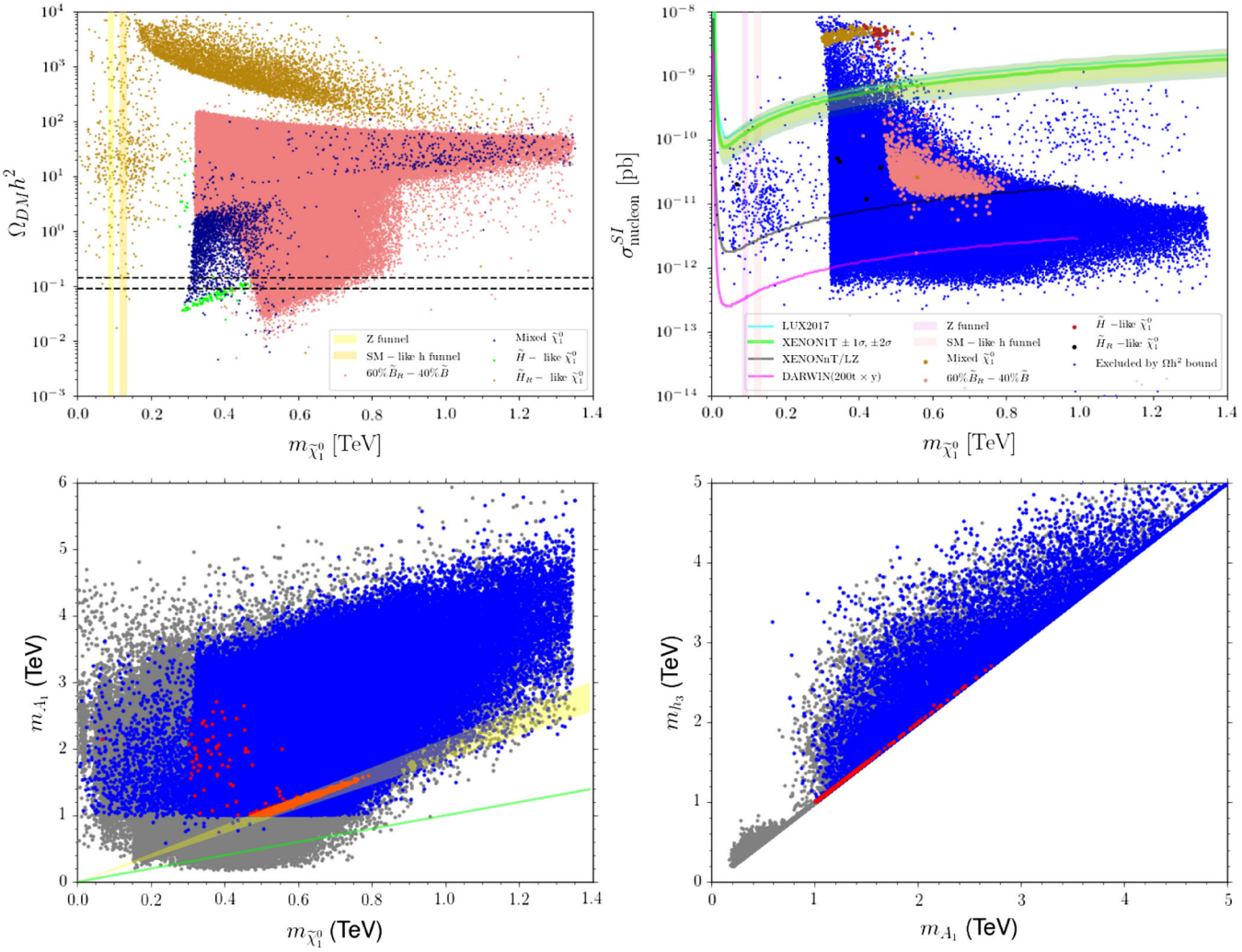

FIG. 4. Dependence of: (top left) the relic density and (top right) spin independent cross section with nuclei on $m_{\tilde{\chi}_1^0}$, (bottom left) the lightest pseudoscalar Higgs mass on $m_{\tilde{\chi}_1^0}$ planes, and (bottom right) the degeneracy between the lightest pseudoscalar mass and the third lightest neutral Higgs boson. Both of these provide the funnel channel for the LSP neutralino annihilation. All points except the dark blue ones are consistent with all constraints as in Table II, while the dark blue ones violate the relic constraints only. The color coding in the $m_{\tilde{\chi}_1^0}-m_{A_1}$ plot is the same as in Fig. 1. The solid line shows the degenerate mass region in these plots. In addition, the shaded region represents A_1 funnel solutions where $m_{A_1}=2m_{\tilde{\chi}_1^0}$ within 8% error.

The $\mu_R - \mu$ plot (bottom right) shows that solutions prefer a positive μ_R to the negative ones, and μ_R can take values in a large range between 500 GeV–7 TeV while the relic density bound can only be fulfilled with the low μ values. As can be seen from $\mu_R - \mu$ plane, the relic density constraint can be satisfied mostly when $\mu \lesssim 0.5$ TeV and 0.7 TeV $\lesssim \mu \lesssim 1.5$ TeV.

The neutralino LSP content consistent with all constraints (including the relic density) is as follows: its mass is constrained as 300 GeV $\lesssim m_{\tilde{\chi}_1^0} \lesssim$ 500 GeV, and for those parameter points, the neutralino LSP content is a $\tilde{B}_R$-ino, $\tilde{H}$-ino and $\tilde{B}$-ino mixture, in this region the wino masses are heavier than the higgsino masses for solutions consistent with the relic density bound. Since $M_1/\mu \lesssim 1$, the bino mixes more than the higgsinos to form the LSP neutralino. In the region 500 GeV $\lesssim m_{\tilde{\chi}_1^0} \lesssim$ 800 GeV, the LPS neutralino is about $60\%\tilde{B}_R - 40\%\tilde{B}$ admixture, consistent also with the top left plot in Fig. 4.

In Fig. 4 we present results specific to dark matter phenomenology, plotting the relic density and spin-independent cross section as a function of the lightest neutralino mass. In addition, we plot the correlation between the lightest pseudoscalar and the third lightest neutral Higgs boson h_3, to highlight the fact that dark matter annihilation proceeds through these two funnels. We show (top left) $\Omega_{\rm DM}h^2 - m_{\tilde{\chi}_1^0}$, (top right) $\sigma^{\rm SI}_{\rm nucleon} - m_{\tilde{\chi}_1^0}$, (bottom left) $m_{A_1} - m_{\tilde{\chi}_1^0}$, and (bottom right) $m_{h_3} - m_{A_1}$ plots. In the top left and top right plane color coding is indicated in the inset, while for the bottom plots the color coding is the same as Fig. 3. The top left plot confirms our previous results on the content of LSP neutralino between 500–800 GeV is composed of 60% $\tilde{B}_R$-ino and 40% $\tilde{B}$-ino, whereas when 300 GeV $\lesssim m_{\tilde{\chi}_1^0} \lesssim$ 500 GeV, its content is shared among $\tilde{B}_R$-ino, $\tilde{H}$-ino and $\tilde{B}$-ino. The top left plot shows the dependence of the relic density, and the right plot shows the dependence of the spin-independent proton and neutron cross section, with neutralino LSP mass. The solid green line represents the current exclusion limit for the XENON1T experiment [46] while yellow and green shaded regions represent solutions within $\pm 1\sigma, \pm 2\sigma$ errors respectively. As can be seen from the graph, most solutions consistent with the relic density constraint can be found below the XENON1T exclusion bound, specifically between 10^{-10} pb—10^{-11} pb. Hence they can be detected by the next generation DM detectors such as XENONnT [47], LZ and DARWIN [48]. Note that we also have a substantial amount of solutions consistent with the relic density above the XENON1T exclusion limit. These solutions correspond to the region where 300 GeV $\lesssim m_{\tilde{\chi}_1^0} \lesssim$ 500 GeV and where the LSP content is either completely $\tilde{H}$-ino or the mixture of $\tilde{B}_R$-ino, $\tilde{H}$-ino and $\tilde{B}$-ino. Thus all solutions surviving consistency with both the current XENON1T exclusion limit and the relic density constraint consist of LSP neutralinos with 500 GeV $\lesssim m_{\tilde{\chi}_1^0} \lesssim$ 800 GeV, and with 60% $\tilde{B}_R$ and 40% $\tilde{B}$ admixture. Finally, the $m_{A_1} - m_{\tilde{\chi}_1^0}$ and $m_{h_3} - m_{A_1}$ plots indicate the funnel channels for the LSP neutralino. The solid green line displays the degenerate mass region for the lightest CP-odd Higgs boson and the LSP neutralino, while the yellow shadowed region indicates solutions with $m_{A_1} = 2m_{\tilde{\chi}_1^0}$, within an 8% error. As can be seen from the graph, the lightest CP-odd Higgs boson, or the neutral h_3 Higgs boson can annihilate into two LSP neutralinos when 450 GeV $\lesssim m_{\tilde{\chi}_1^0} \lesssim$ 800 GeV. Solutions consistent with the relic density constraint can be found when A_1 is degenerate with h_3, with a mass between 1 and 3 TeV. In this energy scale A_1 and h_3 provide the main funnel channels of this model. Apart from these, we have also verified the relation of the relic density with the IceCube confidence level exclusion and the neutrino flux, and all neutralino LSP solutions surviving relic and cross section bounds are within a 1% confidence level of the experimental result.

B. Sneutrino dark matter

The BLRSSM contains, in addition to the three left sneutrinos, six additional singlet states, three right sneutrinos and three $\tilde{S}$, the scalar partners of S. The latter two provide candidates for the sneutrino dark matter, as they do not suffer from a too large annihilation cross section (thus a small relic density) from interacting through Z or W bosons. Sneutrinos thus provide alternative candidates for dark matter in this model, and we analyze their consequences in this section. In the left and right panels of Fig. 5 we show the dependence of the relic density $\Omega_{\rm DM}h^2$ as a function of the lightest scalar neutrino mass. The color bars in the right side of each plot indicate the right-handed sneutrino and the $\tilde{S}$ content, respectively. As can be seen from the plot, even though it is possible to find sneutrino LSP solutions for almost all values of $m_{\tilde{\nu}_1}$ between 0–1400 GeV, requiring consistency with the relic density bound constraints LSP sneutrinos to be between 200–400 GeV. Thus the indication would be that the sneutrino LSP case allows lighter LSP masses compared to the neutralino LSP scenario. The right-handed content of the sneutrino LSP solutions changes between 45%–80%, while the $\tilde{S}$ composition varies between 20%–52%. Imposing relic density bounds, the mixed sneutrino LSP is about 50%–50% between right-handed and $\tilde{S}$. Thus the scalar partner of S, introduced for the neutrino seesaw, plays a crucial role in the sneutrino LSP composition.

In Fig. 6 we analyze the dependence of the nucleon spin-independent cross section, $\sigma_p^{\rm SI}$ for both the proton (left panel) and neutron (right panel). The color coding is the same as Fig. 1 and also indicated in the legend of the plots. The plots show the relation for the spin independent cross section for a proton and neutron respectively. We note that

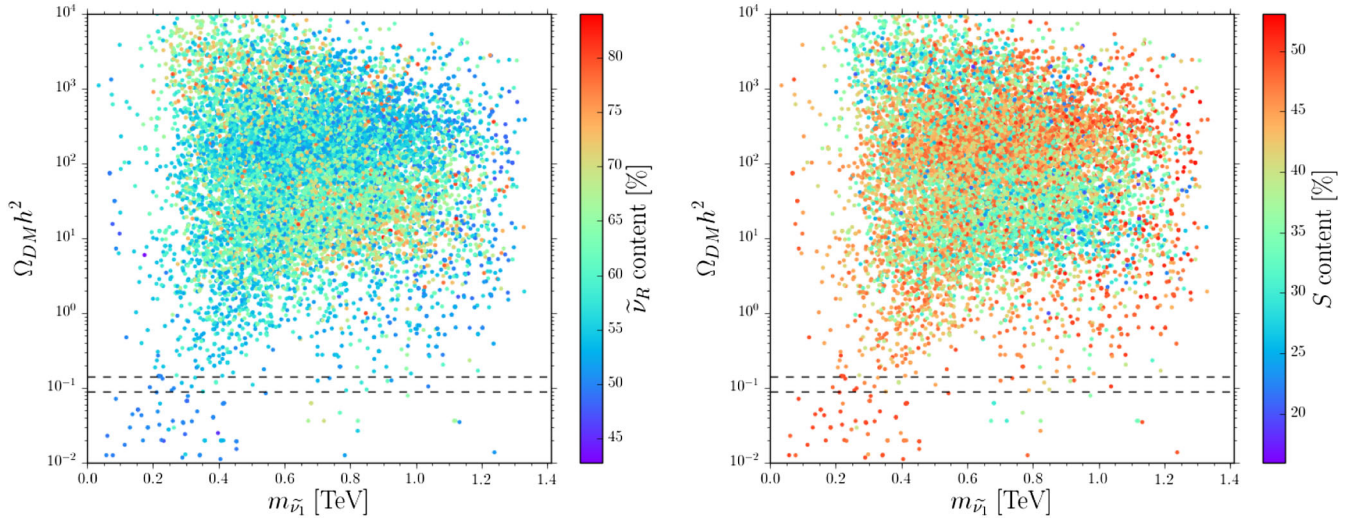

FIG. 5. Dependence of the relic density $\Omega_{\rm DM}h^2$ on the lightest sneutrino mass $m_{\tilde{\nu}_1}$, showing the right sneutrino composition (left panel) and $\tilde{S}$ composition (right panel). All points are consistent with REWSB, LHC bounds, B-physics constraint and sneutrino LSP, while only the points between the two dashed lines satisfy relic density constraints.

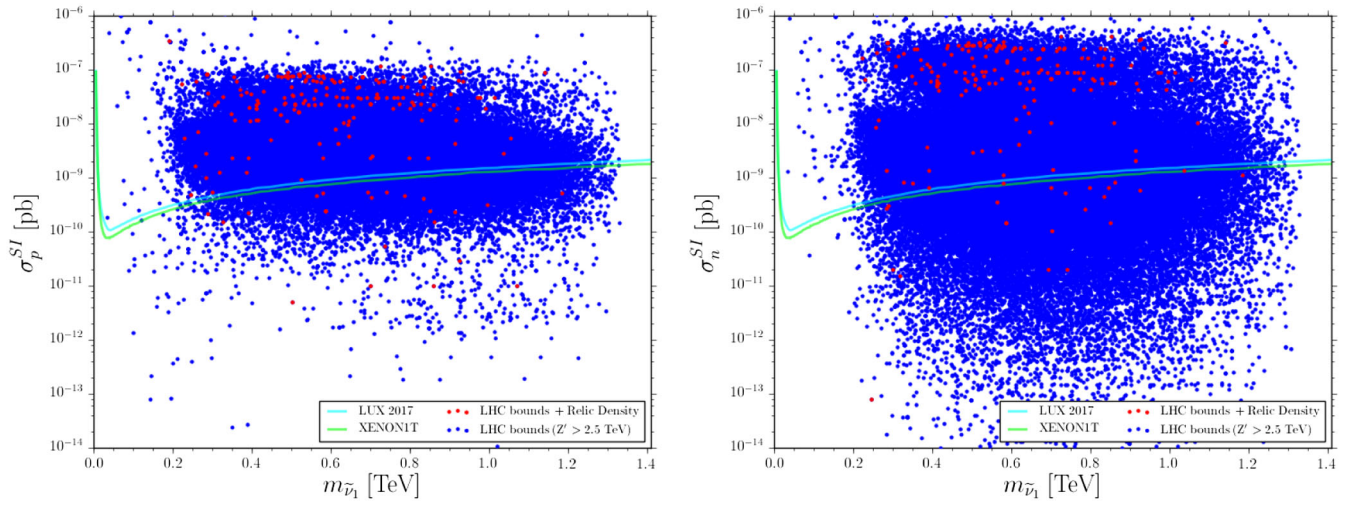

FIG. 6. Dependence of the spin independent cross section for the proton $\sigma_p^{\rm SI}$ (left) and neutron $\sigma_n^{\rm SI}$ (right) as a function on the sneutrino LSP mass $m_{\tilde{\nu}_1}$. All points are consistent with the REWSB and sneutrino LSP. The color coding in each plane is the same as Fig. 1.

both dark matter constraints (the relic density and $\sigma_p^{\rm SI}$) severely restrict the parameter space where the sneutrino is the LSP in this model.

V. COMPARISON OF THE TWO DARK MATTER SCENARIOS

In the previous section, we analyzed dark matter (DM) phenomenology for both neutralino LSP and sneutrino LSP scenarios in the BLRSSM. As discussed in detail, the BLRSSM provides quite a different mass spectrum for two distinct variants of LSP, and these relatively two different mass spectra change the low scale DM phenomenology in an important manner. While we found the sneutrino LSP scenario to be highly constrained and statistically unlikely, there are a few parameter points that survive universal boundary conditions, so in this section, we compare results for the two different LSP scenarios. In Fig. 7 we plot in the $\mu - \mu_R$ and $\tan\beta - M_2/\mu$ dependence. Dark blue points satisfy the mass bounds and constraints from the rare B-decays for the neutralino LSP solutions. Red points form a subset of dark blue, and represent neutralino LSP solutions which satisfy the relic density constraint. Light blue solutions are consistent with the mass bounds and the constraints from the rare B-decays for sneutrino LSP solutions, while yellow points form a subset of light blue, and represent sneutrino LSP solutions consistent with the relic density constraint.

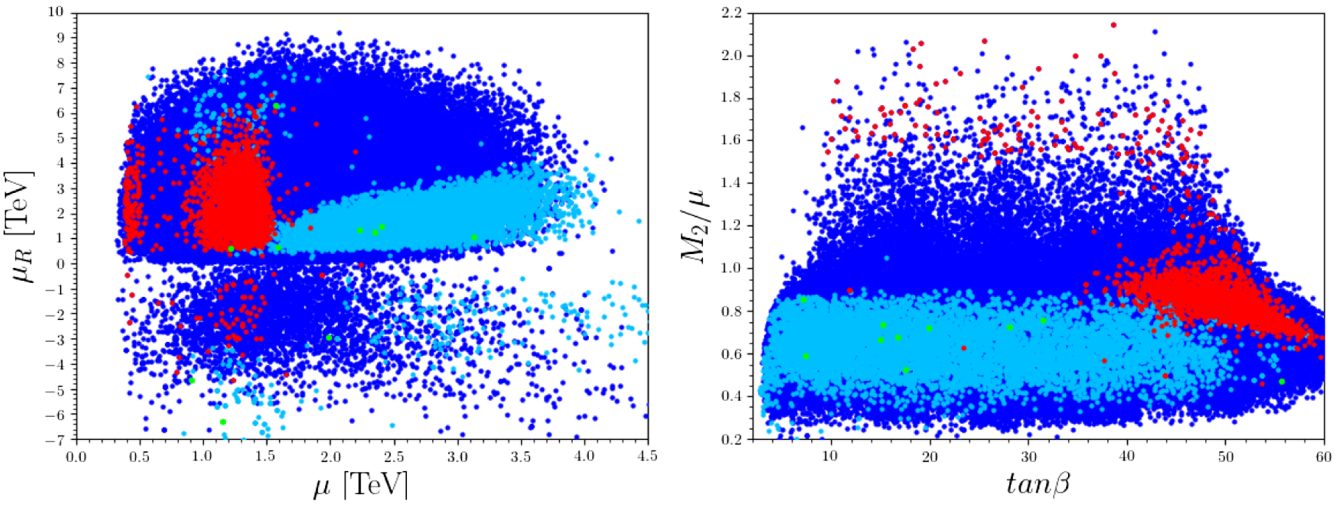

FIG. 7. Dependence of higgsino parameters μ_R and μ (left), and of M_2/μ of $\tan\beta$ (right). All points are consistent with mass bounds, B-physics bounds, HiggsBounds and HiggsSignals. Dark blue points displays neutralino LSP solutions whereas light blue ones stand for sneutrino LSP solutions. Red points represent the neutralino LSP solution, while green ones stand for sneutrino LSP solutions, consistent in addition, with the relic density bound.

The $\mu - \mu_R$ plots compare the higgsino sectors of our model. We note that while the neutralino LSP solution can allow values of μ_R between 0–9 TeV, sneutrino LSP solutions prefer low μ_R values, mainly between 0–4 TeV for a positive μ_R. Even this range becomes narrow, around 1.5 TeV, for lighter higgsinos. For the sneutrino LSP solutions, μ_R values favor the region between 4–7 TeV when $\mu < 1.5$ TeV. On the right panel, the $\tan\beta - M_2/\mu$ plane shows the relative wino and higgsino mass ranges for the two LSP scenarios.

From the plots, we conclude that for a sneutrino LSP, $M_2/\mu \lesssim 1$ and the wino is always lighter than the higgsino over all the parameter space. For the neutralino LSP case, the higgsinos can be lighter or heavier than winos. Also, $\tan\beta$ values for sneutrino LSP solutions are found anywhere in the 0–50 range, and solutions consistent with the relic density constraint can be obtained for either $M_2/\mu \lesssim 1$ or $M_2/\mu \gtrsim 1$. Requiring consistency with the relic density bound solutions with $M_2/\mu \gtrsim 1$ correspond to a neutralino LSP, and $\tan\beta$ values lie in the 10–50 range. Requiring compatibility with the relic density bound, further constrains the region $M_2/\mu \lesssim 1$ to correspond to a $\tilde{B} - \tilde{B}_R$ dominated neutralino LSP solution, where $\tan\beta$ should be between 40–60.

In general the model clearly favors solutions with a neutralino LSP to those with a sneutrino LSP.

A. The neutral Higgs sector

The choice of the LSP affects the heavier states in the Higgs sector of the BLRSSM. For both neutralino and sneutrino LSP solutions, the lightest neutral Higgs boson can be lighter than 150 GeV. Figure 8 shows the results for the values of Higgs masses for both LSP cases with plots for m_{h_2} relative to m_{h_1} (left) and m_{A_1} dependence of $\tan\beta$ (right), where A_1 is the lightest pseudoscalar. The color coding is described in the legend of these planes. The left plot shows that while the two lightest neutral Higgs bosons can be degenerate when the LSP is neutralino, degenerate solutions cannot be obtained for the sneutrino LSP, where the second lightest Higgs boson mass is between 150–700 GeV. This phenomenon can be explained as due to the contributions obtained from different elements of the CP-even Higgs mass matrix. When $m_{h_2} > 150$ GeV, the dominant contribution comes from the m^2_{RR} element of the CP-even Higgs mass matrix, corresponding to singlet Higgs fields associated with $U(1)_R \times U(1)_{B-L}$. Thus there h_2 is mostly a singlet Higgs boson. The off diagonal term m^2_{LR} which provides essential mixing between the two sectors becomes important when $m_{h_2} < 150$ GeV. For the sneutrino LSP solutions, the Yukawa coupling Y_s is constrained to be small (as the sneutrino LSP mass is generated mostly through this term), unlike when the LSP is the neutralino. The Y_s coupling then imposes lighter h_2 masses, mostly generated by the singlet Higgs field $\mathcal{X}_R$. The other Higgs bosons can be quite heavy. This is seen also in the right-hand side of Fig. 8, where we plot the dependence of the mass of the lightest pseudoscalar Higgs boson A_1 (degenerate with h_3), with $\tan\beta$. As before, the region in $\tan\beta \sim 40$–60 represents the mixed binos neutralino LSP solutions, while for $\tan\beta < 40$, regions with a larger (smaller) A_1 mass correspond to a sneutrino (neutralino) LSP. Thus the second lightest Higgs boson is a singlet in both scenarios, but, while the sneutrino LSP scenario favors the 150–700 GeV mass range, for the neutralino LSP solutions the second lightest Higgs boson mass can be much heavier than 700 GeV.

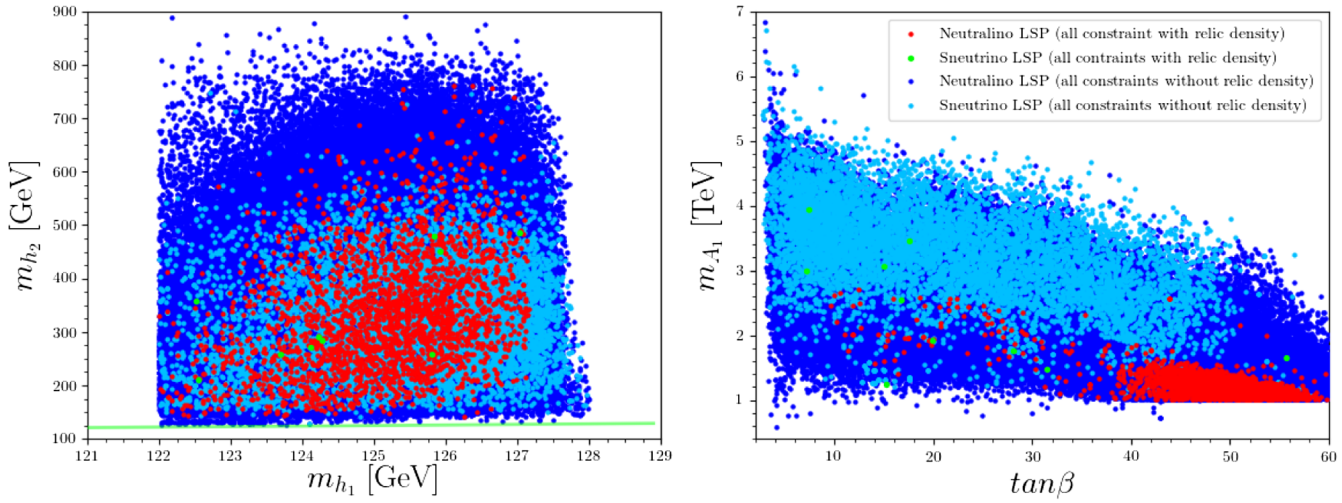

FIG. 8. Dependence of m_{h_2} and m_{h_1} (left) and dependence of m_{A_1} on $\tan\beta$ (right). The color coding is as follows. Dark blue and light blue points represent neutralino LSP and sneutrino LSP solutions respectively, and they both satisfy all experimental bounds illustrated in Table II, except for the relic density bound. In addition, red and green solutions form a subset of dark blue and light blue respectively, and they both represent solutions consistent with the constraints in Table II, including the relic density bound. In addition, the solid green line shows the degenerate mass region where $m_{h_1} = m_{h_2}$.

B. The muon anomalous magnetic moment

The experimental results for the muon anomalous magnetic moment pioneered by the BNL E821 experiment 49,50]] have been improved with the updated results from FNAL E989 [51] and J-PARC E34 [52] experiments. However, the SM prediction for the muon anomalous magnetic moment [53], $a_\mu = (g-2)_\mu/2$, indicates a 3.5σ deviation from the experimental results,

$$\Delta a_\mu = a_\mu^{\rm exp} - a_\mu^{\rm SM} = (28.7 \pm 8.0) \times 10^{-10} (1\sigma) \quad (5.1)$$

The SM prediction is limited in precision by the evaluation of hadronic vacuum polarization contributions. Calculations exist for the lowest contributions, evaluated using perturbative QCD and experimental cross section data involving e^+e^- annihilation into hadrons. However, the large discrepancy has motivated possible explanations within new physics scenarios.

In MSSM, if one of the smuons and bino or wino soft masses can be sufficiently light, supersymmetry can ameliorate this discrepancy. However, if the model is required to obey universality conditions at $M_{\rm GUT}$, obtaining the correct Higgs boson mass is the greatest challenge to explaining the muon $g-2$ anomaly. We can expect better results from the BLRSSM model since it includes an inverse seesaw mechanism and an extra gauge sector. The effect of the inverse seesaw mechanism can be read through RGE for the smuons. As can be seen from the last two terms of Eq. (A7), the Yukawa coupling Y_ν helps decrease the smuon masses at low scales, as compared to models without an inverse seesaw. A similar effect can be read through the RGE of μ Eq. (A1) and sneutrinos Eq. (A6). The presence of another free Yukawa coupling Y_s in addition to Y_ν contributes to evolving light sneutrino masses to the low scale via RGE as can be seen from the Eq. (A6).

Here we investigate the effects on the muon $g-2$ anomaly for both sneutrino and neutralino LSP cases. Figure 9 displays the correlations between a muon a_μ and the relevant free parameters in m_0, $M_{1/2}$, $\tan\beta$ and μ. The color coding is the same as Fig. 8 except that we do not impose the relic density constraint. In addition, the shadowed regions show 1, 2 and 3σ deviations between the calculated contribution to the muon $g-2$ factor and its experimental value. The top left side plot shows that Δa_μ favors low values for m_0 (light scalar masses). Similarly light gaugino masses (light electroweakinos) are also required to decrease the Δa_μ discrepancy, as seen from the top right-handed plot. The need of light scalars and electroweakinos agrees with large $\tan\beta$ values (bottom left panel). Finally, the Δa_μ depends sensitively on the μ parameter, as in MSSM, and here the contribution to the muon $g-2$ factor drops sharply for $\mu > 1.5$ TeV. This is due to one loop contributions effects, where, as the μ term increases, the contributions where the higgsinos run in the loop are suppressed, while the bino-smuon loop is left as only an effective contributing diagram. However, as the bino masses cannot be as low as $\tilde{B}_R$ masses, the contribution from this channel is insufficient. And thus, against expectations, the inverse seesaw mechanism cannot sufficiently enhance the muon Δa_μ within universality conditions, and the corrections hardly reach the 2σ region.

C. Z' mass constraints

To highlight the differences between the two scenarios, we kept the model as general as possible and did not

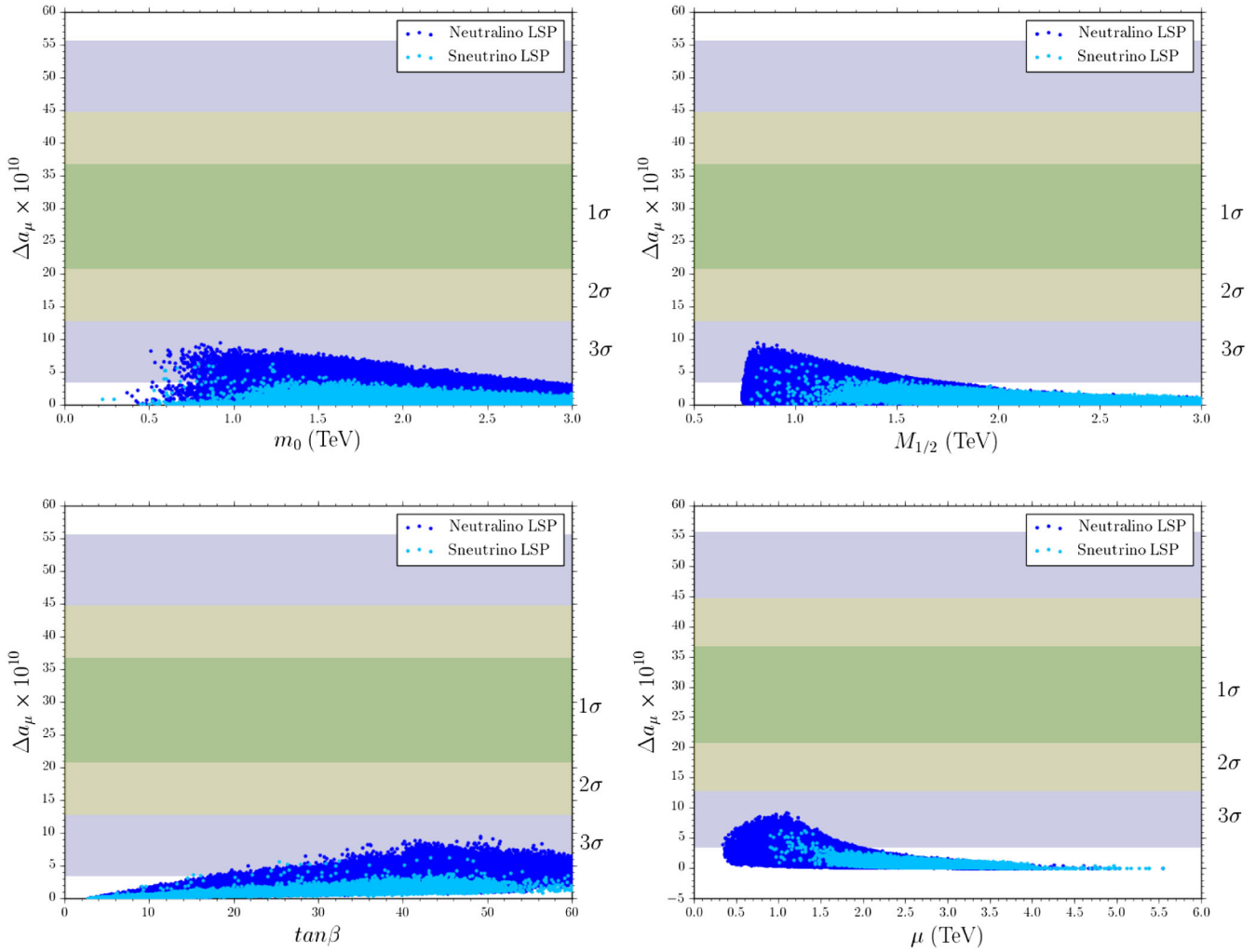

FIG. 9. Δa_μ dependence of m_0 (top left), $M_{1/2}$ (top right), $\tan\beta$ (bottom left) and μ (bottom right). The color coding is the same as Fig. 8, except that the relic density bound is not implemented. In addition, the shadowed regions show 1σ, 2σ and 3σ differences between the theoretical contribution to the muon $g-2$ factor and its experimental value.

impose the latest Z' mass bounds so far. In this section, we include an investigation of implications of the constraints imposed on the Z' mass by a recent new study at ATLAS [11], requiring an increase in the lower bound for the BLRSSM model to $M_{Z'} > 3.9(3.6)$ TeV in the $ee(\mu\mu)$ channels. One must be careful when applying these bounds. First, the experiment assumes nonsupersymmetric models, and thus a case where Z' does not decay to supersymmetric particles, which will modify its total decay width and thus branching ratios. Second, the parameter choice and unification scale are different from ours: the choice depends on symmetry breaking scales and the assumed multiplet composition of the GUT parent. With this note of caution, we explore the parameter space here.

First, we show some of the decay rates of the Z' boson in the BLRSSM. Figure 10 displays some of the important decay channels of Z' where $\mathrm{BR}(Z' \to ll) = \mathrm{BR}(Z' \to ee) + \mathrm{BR}(Z' \to \mu\mu) + \mathrm{BR}(Z' \to \tau\tau) + \mathrm{BR}(Z' \to \nu\nu)$, $\mathrm{BR}(Z' \to \tilde{l}\,\tilde{l})$, $\mathrm{BR}(Z' \to qq)$ and $\mathrm{BR}(Z' \to \tilde{\chi}\tilde{\chi})$, all plots as a function of $m_{Z'}$. Throughout, all points are consistent with LHC, B-physics bounds, HiggsBounds and HiggsSignals. Dark blue points show neutralino LSP solutions whereas light blue ones stand for sneutrino LSP solutions.

The top left panel in Fig. 10 exhibits the branching ratio of Z' into lepton pairs while the top right panel shows the branching for the supersymmetric partners in the same channel. As can be seen from top left plane, the branching ratio of Z' into all leptons ($e^+e^-, \mu^+\mu^-$, $\tau^+\tau^-$ and their neutrinos). changes between 25%–37% while its decays into their supersymmetric partners, sleptons, are low, in the range of 0% and 16%. It is interesting to note that these models, unlike E_6-derived models containing an extra $U(1)'$ gauge group, are not likely to be leptophobic as the branching ratio into leptons is significant throughout the parameter space investigated. The bottom panels of Fig. 10 show the branching ratio into quarks (left) and into neutralinos and/or charginos (right).

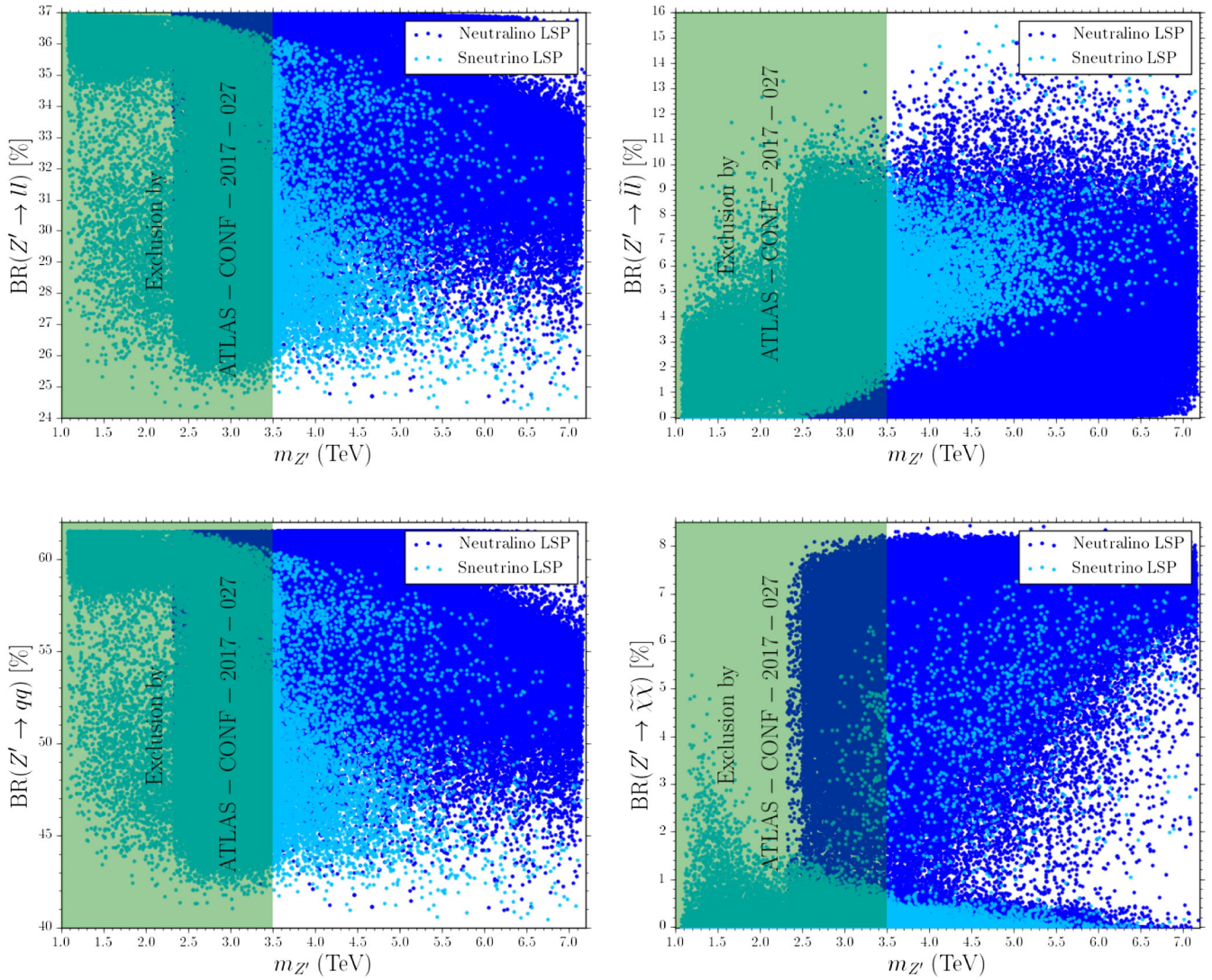

FIG. 10. Branching ratios of Z' in BLRSSM. (Top left): BR($Z' \to ll(ee + \mu\mu + \tau\tau$ and their neutrinos)); (top right) BR($Z' \to \tilde{l}\tilde{l}$), (bottom left) BR($Z' \to q\bar{q}$) and (bottom right) BR($Z' \to \tilde{\chi}\tilde{\chi}$). Neutralino LSP points are represented in dark blue, sneutrino LSP points in light blue. The solutions excluded by [11] are in the shaded green region.

As usual, the largest branching ratio obtained is hadronic (40%–62%), which, though significant, is not as large as for $U(1)'$ models [54], which will likely adversely affect the Z' production cross section. The decay into two charginos or neutralinos occurs above their mass threshold and is very small throughout the whole parameter space (0%–8%). So it appears that the decay of the Z' boson is fairly consistent with a nonsupersymmetric scenario. Based on this, we shall investigate the effects of setting the mass lower bound to be $m_{Z'} > 3.5$ TeV throughout our analyses.

Next, we analyze the likelihood of observing the Z' in hadronic or leptonic decays. In Fig. 11 we plot the production cross section $\sigma(pp \to Z')$ followed by the decay into leptons ($e^+e^- + \mu^+\mu^-$ only, as in the ATLAS [11] results), on the left-hand side, and the same production cross section, followed by the decay into $q\bar{q}$ pairs (excluding top quarks), on the right. We indicate the branching ratios explicitly on the panels at the right-hand side and compare both results with the experimental curves obtained by ATLAS [11] and CMS [55]. Although the dominant decay modes of Z' are into $q\bar{q}$ pairs, the leptonic decays are the most limiting and, in this very much constrained model, the limits on the Z' mass turn out to be closer to 3.75 TeV (at 2σ). Clearly, the model parameters are quite close to this limit, and Z' should be observed with only a small increase in luminosity. For the three benchmarks chosen in Sec. VI, in Table III, we chose the mass of Z' to be close to the experimental limit. The values for $\sigma(pp \to Z') \times \mathrm{BR}(Z' \to ll(ee + \mu\mu))$ are just below the experimental limits, but again, an increase of luminosity of a factor of 2–5 will either show a peak in the curve, or rule this scenario out.

TABLE III. Benchmarks for BLRSSM with relevant cross sections and branching ratios. We include relevant information on the Z' boson and dark matter. In bold, the lightest chargino and the two lightest neutralino states. Missing entries represent values smaller than 10^{-4}.

	Benchmark 1	Benchmark 2	Benchmark 3
m_0 [GeV]	2916	1831	2073
$M_{1/2}$ [GeV]	1159	1092	1166
$\tan\beta$	55.9	45.3	58.6
$\tan\beta_R$	1.15	1.19	1.06
A_0 [GeV]	−16.56	826	1652
$\langle v_R \rangle$ [GeV]	11321	11711	12969
Y_ν $(M_{\rm SUSY})$	0.18	2.11×10^{-3}	0.25
Y_s $(M_{\rm SUSY})$	0.41	0.62	0.49
μ [GeV]	1246	787	1305
μ_R [GeV]	434	1144	3817
$m_{\tilde{\chi}_1^0}$ [GeV]	**428** ($\tilde{H}_R$-like)	**470** (mixed $\tilde{B}_R - \tilde{B}$)	**506** (mixed $\tilde{B}_R - \tilde{B}$)
$m_{\tilde{\chi}_2^0}$ [GeV]	**958**	**768**	**954**
$m_{\tilde{\chi}_1^\pm}$ [GeV]	**507**	**767**	**954**
m_{h_2} [GeV]	428	380	224
m_{h_3} [GeV]	1158	1018	1013
m_{A_1} [GeV]	1175	1020	1017
$m_{\tilde{t}_1}$ [GeV]	2455	1977	2209
$m_{\tilde{b}_1}$ [GeV]	2778	2279	2458
$m_{\tilde{\tau}_1}$ [GeV]	1790	1332	1064
$m_{\tilde{\nu}_1}$ [GeV]	2638	2036	1858
$m_{Z'}$ [GeV]	4046	4182	4632
$m_{\tilde{g}}$ [GeV]	2671	2473	2634
$\sigma(pp \to \tilde{\chi}_1^\pm \tilde{\chi}_2^0)$ [fb]	1.25×10^{-3}	1.27	7.29×10^{-1}
$\sigma(pp \to \tilde{\chi}_1^+ \tilde{\chi}_1^-)$ [fb]	3.9×10^{-1}	7.03×10^{-1}	3.47×10^{-1}
$\sigma(pp \to \tilde{\tau}_1 \tilde{\tau}_1)$ [fb]	4.50×10^{-4}	2.05×10^{-3}	3.46×10^{-3}
$\mathrm{BR}(\tilde{\chi}_2^0 \to \tilde{\chi}_1^0 h_1)$	⋯	0.94	0.89
$\mathrm{BR}(\tilde{\chi}_1^\pm \to \tilde{\chi}_1^0 W^\pm)$	⋯	0.99	0.99
$\mathrm{BR}(\tilde{\tau}_1 \to \tau_1 \tilde{\chi}_1^0)$	⋯	0.51	0.99
$\sigma(pp \to Z' \to q\bar{q})$ [fb]	5.75×10^{-1}	4.24×10^{-1}	1.61×10^{-1}
$\sigma(pp \to Z' \to e^+e^- + \mu^+\mu^-)$ [fb]	1.31×10^{-1}	9.67×10^{-2}	3.68×10^{-2}
$\mathrm{BR}(Z' \to e^+e^- + \mu^+\mu^-)$	0.12	0.12	0.12
$\mathrm{BR}(Z' \to e^+e^- + \mu^+\mu^- + \tau^+\tau^-)$	0.18	0.18	0.18
$\mathrm{BR}(Z' \to \nu\bar{\nu})$	0.16	0.16	0.15
$\mathrm{BR}(Z' \to q\bar{q})$	0.56	0.56	0.55
$\mathrm{BR}(Z' \to \tilde{l}\,\tilde{l})$	4.01×10^{-4}	3.54×10^{-3}	2.07×10^{-2}
$\mathrm{BR}(Z' \to \tilde{q}\,\tilde{q})$	⋯	1.79×10^{-4}	1.38×10^{-4}
$\mathrm{BR}(Z' \to \tilde{\chi}\,\tilde{\chi})$	7.64×10^{-2}	8.06×10^{-2}	7.33×10^{-2}
Ωh^2	0.1369	0.0978	0.0958
$\sigma^{\rm SI}_{\rm nucleon}$ [pb]	1.60×10^{-11}	1.80×10^{-10}	2.43×10^{-11}
$\sigma^{\rm SD}_{\rm p}$ [pb]	4.68×10^{-8}	1.12×10^{-6}	6.72×10^{-8}
$\sigma^{\rm SD}_{\rm n}$ [pb]	4.31×10^{-8}	9.15×10^{-7}	6.38×10^{-8}
Icecube22 Exclusion CL [%]	1.15×10^{-2}	0.65	3×10^{-2}
$\langle \sigma v \rangle$ [cm^3 s^{-1}]	2.12×10^{-26}	1.33×10^{-26}	3.07×10^{-26}
Φ_ν [km$^2 y^{-1}$]	2.39×10^6	1.70×10^8	6.97×10^6
Φ_μ [km$^2 y^{-1}$]	2.28×10^{-2}	1.37	6.16×10^{-2}
Φ_γ [cm^2 s GeV]$^{-1}$	9.25×10^{-16}	8.42×10^{-16}	1.85×10^{-15}
Annihilation modes			
$\tilde{\chi}_1^0 \tilde{\chi}_1^0 \to b\bar{b}$	76%	74%	75%
$\tilde{\chi}_1^0 \tilde{\chi}_1^0 \to \tau^+\tau^-$	23%	20%	24%
$\tilde{\chi}_1^0 \tilde{\chi}_1^0 \to h_1 Z$	⋯	6%	⋯

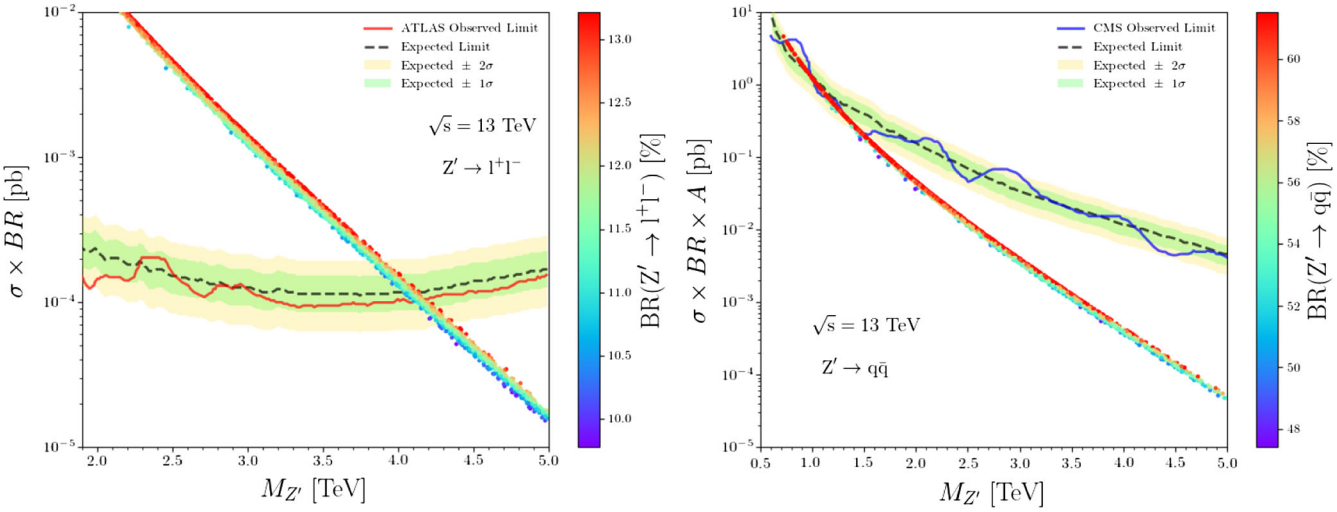

FIG. 11. Cross sections times branching ratios of Z' in BLRSSM. (Left): $\sigma(pp \to Z') \times \mathrm{BR}(Z' \to ll(ee + \mu\mu))$; (right) $\sigma(pp \to Z') \times \mathrm{BR}(Z' \to q\bar{q})$, with branching ratios values only shown in the right-sided panels. The experimental results from by ATLAS [11] (left) and CMS [55] (right), are shown as red curves, with 1σ deviation shaded in green and 2σ deviation shaded in yellow.

VI. COLLIDER SIGNALS AND DARK MATTER DETECTION

With the constraints on the Z' mass from the previous section, we revisit the plots for the spin independent cross section for a proton and neutron respectively. While in the Fig. 6, we considered $m_{Z'} \geq 2.5$ TeV, and the spin-independent proton (or neutron) cross sections for sneutrino LSP solutions were satisfied with the XENON1T experimental exclusion limit, imposing the new Z' mass limit excludes most of the parameter space for sneutrino LSP solutions, as shown in Fig. 12. Specifically, of about 10^6 scanned parameter points only 18 solutions compatible with the relic density bound are found, and only ten of them can survive the XENON1T experimental exclusion limit. Imposing Z' mass constraints, the sneutrino LSP scenario thus emerges as extremely constrained and, realistically, ruled out. However, the neutralino LSP scenario is unaffected by the Z' mass limits and survives direct detection constraints, as in Fig. 4.

In addition to *direct detection*, DM searches also attempt to identify visible products resulting from DM interactions, focusing on searching for SM particles produced by the decay or annihilation of DM. These are *indirect searches*, and the advantages of these are the large amounts of available DM, while the challenges are that the DM interacts weakly with SM particles, so the rate of production of these particles is expected to be small. In our model,

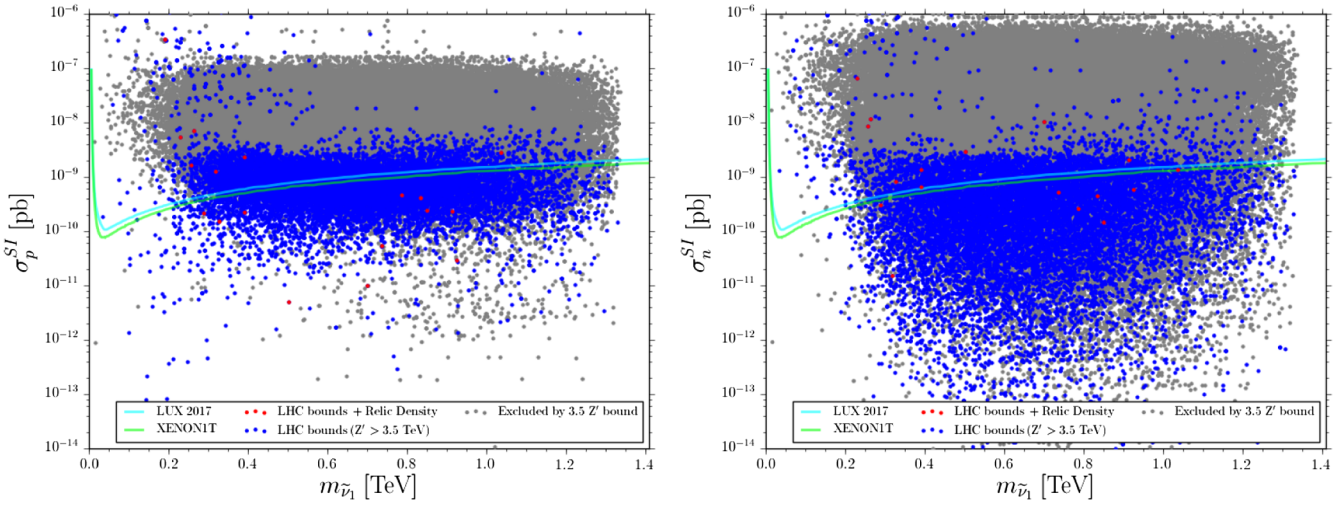

FIG. 12. Dependence of the spin independent cross section for the proton σ_p^{SI} (left) and neutron σ_n^{SI} (right) as a function on the sneutrino LSP mass $m_{\tilde{\nu}_1}$, for, $m_{Z'} \geq 3.5$ TeV. All points are consistent with REWSB and sneutrino LSP. The color coding in each plane is the same as Fig. 1.

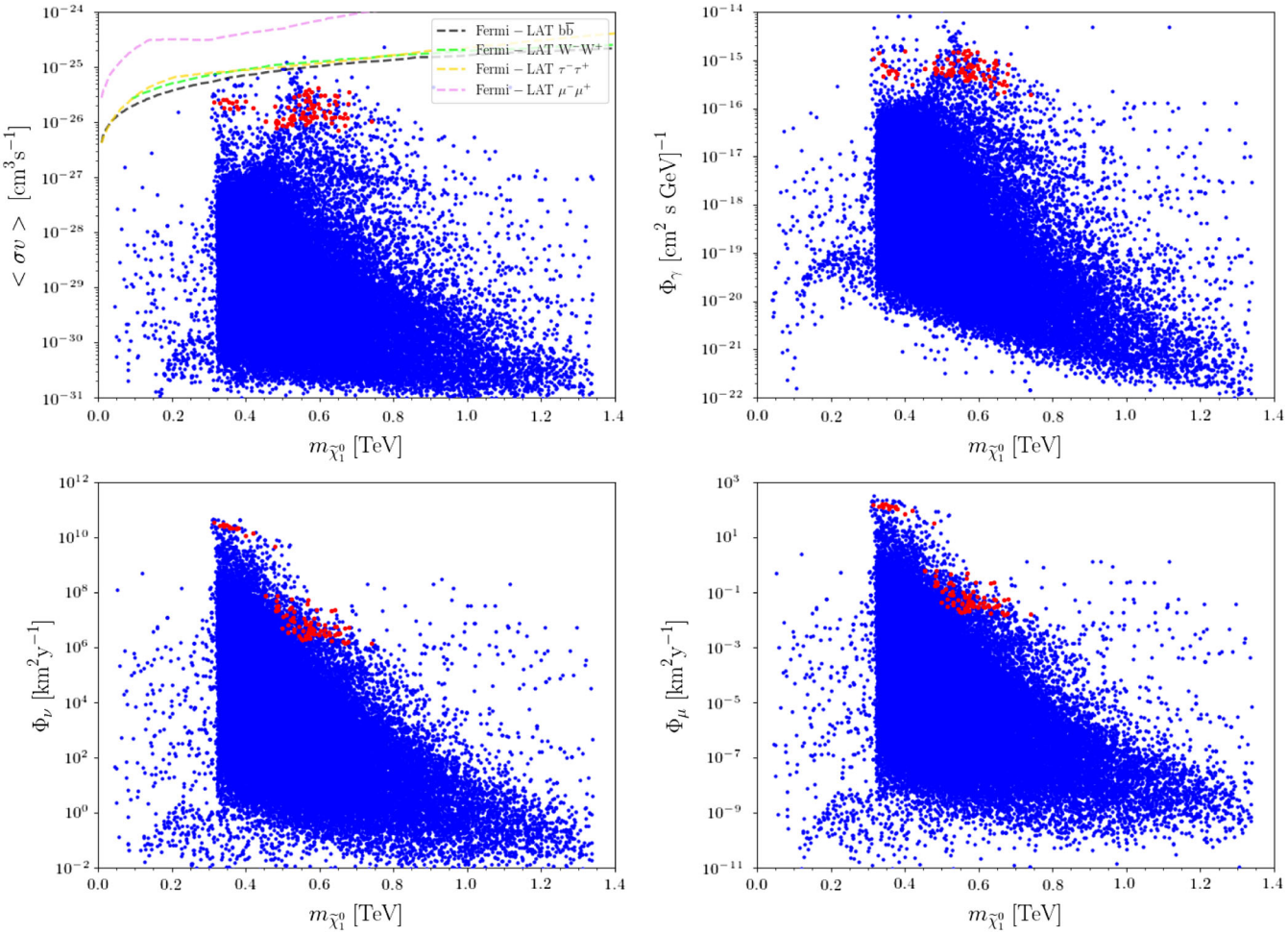

FIG. 13. (Top left): Annihilation cross section of DM as a function of the LSP neutralino mass, and compare it with the constraints from $\mu^+\mu^-$ (pink dotted line), $\tau^+\tau^-$ (yellow dotted line), W^+W^- (green dotted line), and $b\bar{b}$ (black dotted line), derived from the combined analysis from Fermi-LAT experiment [56]; (top right): Photon flux as a function of the LSP neutralino mass; (bottom left): Neutrino flux as a function of the LSP neutralino mass; (bottom right): Muon flux as a function of the LSP neutralino mass. As before, the regions in red satisfy all constraints, including relic density.

R-parity is exact and the DM is stable, however DM can annihilate into leptons, hadrons and W^+W^- pairs. We plot, in Fig. 13, left top panel, the annihilation cross section of DM as a function of the LSP neutralino mass, and compare it with the constraints from $\mu^+\mu^-$ (pink dotted line), $\tau^+\tau^-$ (yellow dotted line), W^+W^- (green dotted line), and $b\bar{b}$ (black dotted line), derived from the combined analysis from the Fermi-LAT experiment [56].[1] As before, the regions in red satisfy all constraints, including for the relic density, and they lie below the exclusion curves. The dominant annihilation decays of DM are into $b\bar{b}$ and $\tau^+\tau^-$, and in Table III, we give branching ratios for the specific benchmarks chosen. Since solutions consistent with the relic density (the red points) are close to the Fermi-LAT experimental curves, we included these in the annihilation cross section plot. However, for both the neutrino flux and muon flux (bottom panels), our results are small compared to the experimental Fermi-LAT results [56]. Specifically, our values for the neutrino flux are changing between 10^6–10^{10} km^2/year, while experimental results for the neutrino flux are between 10^{10}–10^{14} km^2/year [58]. Similarly, our values for the muon flux are between 10^{-2}–10^3 km^2/year, while experimental results for the muon flux are between 10^2–10^5 km^2/year [59]. Finally, we show the photon flux result (top right panel), which changes between 10^{-14}–10^{-22} km^2/year, and which is tiny and does not explain the γ-ray excess from the Galactic center (GC) detected by Fermi-LAT, for photons between 20 MeV and 300 GeV. We include exact values for the fluxes for our benchmarks in Table III.

Lastly, we would like to analyze the production and decays for this scenario at the LHC. We choose benchmarks from the parameter scan results which satisfy all

[1]Comparably strong limits come also from AMS-02 [57] and the cosmic microwave background.

experimental bounds, including the relic density constraint and XENON1T exclusion limits, and favor light neutralino LSP solutions as the only ones surviving all constraints. We proceed by exporting the BLRSSM to the UFO format [60] and use the MG5_aMC@NLO framework version 2.5.5 [61] to simulate hard-scattering LHC collisions and evaluate the cross sections for various signals. For the calculation of cross sections, we select three benchmarks with different features, which could showcase different features of the model for detection at the LHC.

The first benchmark, benchmark 1 has a $H_{\tilde{R}}$-like neutralino LSP. (Even though parameter scans allow Higgsino-like and higgsino-binos mixed LSP neutralino solutions between 300–500 GeV, no benchmark in this range can be found as these states are completely excluded by the XENON1T exclusion limit.) We thus select benchmarks with mixed $\tilde{B}_R - \tilde{B}$ content. For benchmarks 2–3, $\mathrm{BR}(\tilde{\chi}_2^0 \to \tilde{\chi}_1^0 h_1)$ and $\mathrm{BR}(\tilde{\chi}_1^\pm \to \tilde{\chi}_1^0 W^\pm)$ are almost unity. Sparticle masses are similar in both cases, with the exception of the lightest chargino, which is heavier for benchmark 3. Also, for benchmark 3, $\mathrm{BR}(\tilde{\tau}_1 \to \tau_1 \tilde{\chi}_1^0) \sim 1$ while this is much smaller for benchmark 2. Note that benchmarks satisfy all the constraints, including the IceCube22 [62] exclusion. Our results are shown in Table III.

Even though the LSP neutralino mass is quite light (428 GeV) for benchmark 1, we find that both chargino-chargino and neutralino-chargino production cross sections are quite low, due to the fact that the neutralino is mostly $\tilde{H}_R$-like. For the other benchmarks, with neutralino contents of mixed binos, the second lightest neutralino and chargino masses are degenerate. We estimated the cross sections for the chargino/neutralinos and stau production as being the most promising. The highest cross section values for the chargino-chargino production and the chargino-neutralino production are obtained for benchmark 2 whose neutralino and chargino masses are 470 GeV and 767 GeV, respectively. As can be seen from the Table III, the chargino-chargino production and neutralino-chargino production cross sections are 7.03×10^{-1} fb and 1.27 fb, respectively. The cross section values decrease in benchmark 3 (with respect to benchmark 2) when neutralino and chargino masses are 506 GeV and 954 GeV (versus 470 and 767 GeV), respectively. For all benchmarks, Z' masses are above 4 TeV, consistent with the latest ATLAS result, but very close to the exclusion limit, as discussed in the previous section, V C. Note that gluino masses are about 2.5 TeV for all benchmarks, making gluino results testable at the HL-LHC or by the next generation colliders [63,64].

Including all the constraints, we conclude that the production of supersymmetric particles in the BLRSSM fall below detector sensitivity. Especially because the final signals will have even lower production cross sections, as they will be suppressed by branching ratios of the chargino/neutralinos to missing energy + leptons. A way to improve our results is to relax some or most universality constraints and looking for effective cuts which would enhance the signal over the background. We shall return to this in a future work.

VII. SUMMARY AND CONCLUSION

We analyzed the predictions of the mass spectrum in the BLRSSM framework with a universal boundary condition, highlighting the solutions consistent with the DM restrictions (the relic density and spin independent cross sections with nucleons) for both neutralino and sneutrino LSP scenarios. We found that the stop and sbottom masses are between 2–3 TeV, and the chargino can be degenerate with the LSP neutralino between 300–500 GeV. In addition, the relic density constraint can be satisfied for masses in the range $300 \lesssim m_{\tilde{\chi}_1^0} \lesssim 800$ GeV. $\tilde{H}$ dominated or a mixed LSP neutralino solution can be obtained below 300 GeV; however these solutions are ruled out by the XENON1T spin independent cross section exclusion curve. When all DM constraints are taken into account, the model favors LSP neutralinos with masses between $500 \lesssim m_{\tilde{\chi}_1^0} \lesssim 800$ GeV, bino-dominated, and with composition 60% $\tilde{B}_R$–40% $\tilde{B}$. We also showed that, when the LSP is neutralino, A_1 and h_3 are funnel channels for pair-producing them.

In addition, the model allows in principle a sneutrino LSP where its content can be either right-handed dominated or mixed, $\tilde{\nu}_R$ and $\tilde{S}$, with masses between 250–1300 GeV. In this sense, sneutrino LSP solutions can be lighter than the neutralino LSP ones. Purely right-handed dominated sneutrino LSP solutions have difficulty to satisfy the relic density constraint and only mixed ones survive. In addition most of the sneutrino LSP solutions are consistent with the XENON 1T spin independent cross section exclusion curve. However, strict imposition of the Z' mass bounds basically rule out the sneutrino solutions, while not having any effect on the neutralino LSP parameter space. This is one of the most important predictions of the model.

The parameter spaces corresponding to the neutralino and sneutrino are quite different. If allowed, sneutrino LSP solutions favor a low singlet higgsino mass parameter, μ_R, and the second lightest neutral Higgs boson as a singlet, while the neutralino LSP favor larger μ_R parameters. Sneutrino LSP solutions are spread out over the whole range of $\tan\beta$, while neutralino solutions are restricted in the $40 \lesssim \tan\beta \lesssim 60$. Neutralino LSP solutions allow for degenerate masses of the two lightest neutral Higgs bosons, while the sneutrino LSP, although favoring a light m_{h_2}, does not. The anomaly in the anomalous magnetic moment of the muon favors neutralino LSP contributions, where for a large range of scalar masses, and a more restricted one for gauginos and higgsinos, the corrections are within 2σ of the experimental result, while sneutrino LSP solutions can at best produce results within 3σ of the desired values.

We analyzed collider signatures of this proposed scenario, including all constraints, and they are not promising, even at the high-luminosity LHC. The largest cross sections are obtained for the chargino/neutralino production, and they are at most of $\mathcal{O}(1)$ fb, without including cascade decays into leptons which would reduce them further. In the future, collider signals could be enhanced by relaxing some of the severe constraints on the model, such as the universality conditions, and finding suitable cuts to enhance signal versus background. This may extend the parameter space, allowing the sneutrino LSP back into the consideration. Work in these directions is underway.

However, under the present scenario, the Z' mass lies just below the sensitivity of LHC at 36 fb^{-1} and would be seen during the LHC run 2, with a modest increase in luminosity. For dark matter detection, direct searches remain the most promising. Projected sensitivities of XENONnT and particularly of DARWIN(200t × y) would observe or rule out the most promising region of neutralino LSP candidates (500–800 GeV). These features are hopeful indicators for the accessibility of the BLRSSM model in the near future.

ACKNOWLEDGMENTS

Part of the numerical calculations reported in this paper was performed using the National Academic Network and Information Center (ULAKBIM) of TUBITAK, High Performance and Grid Computing Center (TRUBA resources), and using High Performance Computing (HPC), managed by Calcul Québec and Compute Canada. We acknowledge NSERC for partial financial support under Grant No. SAP105354.

APPENDIX: RENORMALIZATION GROUP EQUATIONS

We gather below some of the relevant equation referred to in the paper.

$$\beta_{\mu}^{(1)} = \mu(-3g_L^2 + 3\mathrm{Tr}(Y_d Y_d^\dagger) + 3\mathrm{Tr}(Y_u Y_u^\dagger) - g_R^2 - g_{RB}^2 + \mathrm{Tr}(Y_e Y_e^\dagger) + \mathrm{Tr}(Y_v Y_v^\dagger)). \tag{A1}$$

$$\beta_{\mu_R}^{(1)} = -\frac{1}{2}\mu_R(2g_R^2 + 2g_{RB}^2 - 2\sqrt{6}g_{BL}g_{RB} - 2\sqrt{6}g_{BR}g_R + 3g_{BL}^2 + 3g_{BR}^2 - 2\mathrm{Tr}(Y_s Y_s^\dagger)). \tag{A2}$$

$$\begin{aligned}\beta_{B_\mu}^{(1)} = {} & +B_\mu(-3g_L^2 + 3\mathrm{Tr}(Y_d Y_d^\dagger) + 3\mathrm{Tr}(Y_u Y_u^\dagger) - g_R^2 - g_{RB}^2 + \mathrm{Tr}(Y_e Y_e^\dagger) + \mathrm{Tr}(Y_v Y_v^\dagger)) \\ & + 2\mu(2g_R g_{RB} M_{BR} + 3g_L^2 M_2 + 3\mathrm{Tr}(Y_d^\dagger T_d) + 3\mathrm{Tr}(Y_u^\dagger T_u) + g_R^2 M_4 + g_{RB}^2 M_1 + \mathrm{Tr}(Y_e^\dagger T_e) + \mathrm{Tr}(Y_v^\dagger T_\nu)).\end{aligned} \tag{A3}$$

$$\begin{aligned}\beta_{B_{\mu_R}}^{(1)} = {} & +B_{\mu_R}\left(-\frac{3}{2}g_{BL}^2 - \frac{3}{2}g_{BR}^2 - g_R^2 - g_{RB}^2 + \sqrt{6}g_{BL}g_{RB} + \sqrt{6}g_{BR}g_R + \mathrm{Tr}(Y_s Y_s^\dagger)\right) \\ & + \mu_R(3g_{BL}^2 M_1 + 2g_{RB}^2 M_1 - 2\sqrt{6}g_{BR}g_{RB}M_{BR} + 4g_R g_{RB} M_{BR} - 2g_{BL}(-3g_{BR}M_{BR} + \sqrt{6}g_{RB}M_1 + \sqrt{6}g_R M_{BR}) \\ & + 3g_{BR}^2 M_4 - 2\sqrt{6}g_{BR}g_R M_4 + 2g_R^2 M_4 + 2\mathrm{Tr}(Y_s^\dagger T_s)).\end{aligned} \tag{A4}$$

$$\begin{aligned}\beta_{m_{H_u}^2}^{(1)} = {} & -2g_R^2|M_4|^2 - 6g_L^2|M_2|^2 - 2g_{RB}(g_{RB}M_1 + g_R M_{BR})M_1^* - 2(g_R^2 M_{BR} + g_{RB}^2 M_{BR} + g_R g_{RB}(M_1 + M_4))M_{BR}^* \\ & - 2g_R g_{RB} M_{BR} M_4^* + g_{RB}\sigma_{1,1} + g_R\sigma_{1,3} + 6m_{H_u}^2\mathrm{Tr}(Y_u Y_u^\dagger) + 2m_{H_u}^2\mathrm{Tr}(Y_v Y_v^\dagger) + 6\mathrm{Tr}(T_u^* T_u^T) + 2\mathrm{Tr}(T_\nu^* T_\nu^T) \\ & + 2\mathrm{Tr}(m_l^2 Y_v^\dagger Y_v) + 6\mathrm{Tr}(m_q^2 Y_u^\dagger Y_u) + 6\mathrm{Tr}(m_u^2 Y_u Y_u^\dagger) + 2\mathrm{Tr}(m_\nu^2 Y_v Y_v^\dagger).\end{aligned} \tag{A5}$$

$$\begin{aligned}\beta_{m_\nu^2}^{(1)} = {} & -3g_{BR}^2\mathbf{1}|M_4|^2 + 2\sqrt{6}g_{BR}g_R\mathbf{1}|M_4|^2 - 2g_R^2\mathbf{1}|M_4|^2 + (-3g_{BL}^2 M_1 + g_{BL}(2\sqrt{6}g_{RB}M_1 - 3g_{BR}M_{BR} + \sqrt{6}g_R M_{BR}) \\ & + g_{RB}(-2g_{RB}M_1 - 2g_R M_{BR} + \sqrt{6}g_{BR}M_{BR}))\mathbf{1}M_1^* + (-3g_{BL}^2 M_{BR} - 3g_{BR}^2 M_{BR} + \sqrt{6}g_{BR}(2g_R M_{BR} \\ & + g_{RB}(M_1 + M_4)) - 2(g_R^2 M_{BR} + g_{RB}^2 M_{BR} + g_R g_{RB}(M_1 + M_4)) + g_{BL}(-3g_{BR}(M_1 + M_4) \\ & + \sqrt{6}(2g_{RB}M_{BR} + g_R(M_1 + M_4))))\mathbf{1}M_{BR}^* - 3g_{BL}g_{BR}M_{BR}\mathbf{1}M_4^* + \sqrt{6}g_{BL}g_R M_{BR}\mathbf{1}M_4^* \\ & + \sqrt{6}g_{BR}g_{RB}M_{BR}\mathbf{1}M_4^* - 2g_R g_{RB}M_{BR}\mathbf{1}M_4^* + \sqrt{\frac{3}{2}}g_{BL}\mathbf{1}\sigma_{1,1} - g_{RB}\mathbf{1}\sigma_{1,1} + \sqrt{\frac{3}{2}}g_{BR}\mathbf{1}\sigma_{1,3} - g_R\mathbf{1}\sigma_{1,3} \\ & + 2m_\chi^2 Y_s Y_s^\dagger + 4m_{H_u}^2 Y_v Y_v^\dagger + 2T_s T_s^\dagger + 4T_\nu T_\nu^\dagger + m_\nu^2 Y_s Y_s^\dagger + 2m_\nu^2 Y_v Y_v^\dagger + 2Y_s m_S^2 Y_s^\dagger + Y_s Y_s^\dagger m_\nu^2 \\ & + 4Y_v m_l^2 Y_v^\dagger + 2Y_v Y_v^\dagger m_\nu^2.\end{aligned} \tag{A6}$$

$$\beta^{(1)}_{m_l^2} = -3g_{BR}^2\mathbf{1}|M_4|^2 - 6g_L^2\mathbf{1}|M_2|^2 - 3g_{BL}(g_{BL}M_1 + g_{BR}M_{BR})\mathbf{1}M_1^* - 3(g_{BL}^2 M_{BR} + g_{BL}g_{BR}(M_1 + M_4) + g_{BR}^2 M_{BR})\mathbf{1}M_{BR}^*$$
$$- 3g_{BL}g_{BR}M_{BR}\mathbf{1}M_4^* - \sqrt{\frac{3}{2}}g_{BL}\mathbf{1}\sigma_{1,1} - \sqrt{\frac{3}{2}}g_{BR}\mathbf{1}\sigma_{1,3} + 2m_{H_d}^2 Y_e^\dagger Y_e + 2m_{H_u}^2 Y_\nu^\dagger Y_\nu + 2T_e^\dagger T_e + 2T_\nu^\dagger T_\nu + m_l^2 Y_e^\dagger Y_e$$
$$+ m_l^2 Y_\nu^\dagger Y_\nu + 2Y_e^\dagger m_e^2 Y_e + Y_e^\dagger Y_e m_l^2 + 2Y_\nu^\dagger m_\nu^2 Y_\nu + Y_\nu^\dagger Y_\nu m_l^2. \quad \text{(A7)}$$

[1] H. E. Haber and M. Sher, Higgs mass bound in $E(6)$ based supersymmetric theories, Phys. Rev. D **35**, 2206 (1987).
[2] M. Cvetic, D. A. Demir, J. R. Espinosa, L. L. Everett, and P. Langacker, Electroweak breaking and the mu problem in supergravity models with an additional U(1), Phys. Rev. D **56**, 2861 (1997).
[3] E. Ma, Exceeding the MSSM Higgs mass bound in a special class of U(1) gauge models, Phys. Lett. B **705**, 320 (2011).
[4] R. N. Mohapatra and A. Rasin, Simple Supersymmetric Solution to the Strong *CP* Problem, Phys. Rev. Lett. **76**, 3490 (1996).
[5] R. N. Mohapatra and G. Senjanovic, Neutrino masses and mixings in gauge models with spontaneous parity violation, Phys. Rev. D **23**, 165 (1981).
[6] J. Schechter and J. W. F. Valle, Neutrino masses in $\mathrm{SU}(2) \times \mathrm{U}(1)$ theories, Phys. Rev. D **22**, 2227 (1980).
[7] J. Schechter and J. W. F. Valle, Neutrino decay and spontaneous violation of lepton number, Phys. Rev. D **25**, 774 (1982).
[8] M. Malinsky, J. C. Romao, and J. W. F. Valle, Novel Supersymmetric SO(10) Seesaw Mechanism, Phys. Rev. Lett. **95**, 161801 (2005).
[9] V. De Romeri, M. Hirsch, and M. Malinsky, Soft masses in SUSY SO(10) GUTs with low intermediate scales, Phys. Rev. D **84**, 053012 (2011).
[10] M. Hirsch, W. Porod, L. Reichert, and F. Staub, Phenomenology of the minimal supersymmetric $U(1)_{B-L} \times U(1)_R$ extension of the standard model, Phys. Rev. D **86**, 093018 (2012).
[11] ATLAS Collaboration and T. A. Collaboration, Report No. ATLAS-CONF-2017-027.
[12] G. W. Bennett *et al.* (Muon g-2 Collaboration), Final report of the muon E821 anomalous magnetic moment measurement at BNL, Phys. Rev. D **73**, 072003 (2006).
[13] M. Hirsch, M. Malinsky, W. Porod, L. Reichert, and F. Staub, Hefty MSSM-like light Higgs in extended gauge models, J. High Energy Phys. 02 (2012) 084.
[14] R. N. Mohapatra and A. Rasin, A supersymmetric solution to *CP* problems, Phys. Rev. D **54**, 5835 (1996).
[15] L. D. Rose, S. Khalil, S. J. D. King, C. Marzo, S. Moretti, and C. S. Un, Naturalness and Dark Matter Properties of the BLSSM, in *25th International Workshop on Deep Inelastic Scattering and Related Topics (DIS 2017) Birmingham, UK, 2017*, arXiv:1706.01301.
[16] C. S. Un and O. Ozdal, Mass spectrum and Higgs profile in BLSSM, Phys. Rev. D **93**, 055024 (2016).
[17] L. Basso, The Higgs sector of the minimal SUSY $B-L$ model, Adv. High Energy Phys. **2015**, 980687 (2015).
[18] W. Abdallah and S. Khalil, Dark matter in BL supersymmetric standard model with inverse seesaw, J. Cosmol. Astropart. Phys. 04 (2017) 016.
[19] S. Khalil and C. S. Un, Muon anomalous magnetic moment in SUSY B-L model with inverse seesaw, Phys. Lett. B **763**, 164 (2016).
[20] S. Khalil and S. Moretti, The $B-L$ supersymmetric standard model with inverse seesaw at the Large Hadron Collider, Rep. Prog. Phys. **80**, 036201 (2017).
[21] W. Porod, SPheno, a program for calculating supersymmetric spectra, SUSY particle decays and SUSY particle production at e^+e^- colliders, Comput. Phys. Commun. **153**, 275 (2003).
[22] W. Porod and F. Staub, SPheno 3.1: Extensions including flavour, *CP*-phases and models beyond the MSSM, Comput. Phys. Commun. **183**, 2458 (2012).
[23] F. Staub, SARAH, arXiv:0806.0538.
[24] F. Stub, Automatic calculation of supersymmetric renormalization group equations, self energies, Comput. Phys. Commun. **182**, 808 (2011).
[25] V. Lucas and S. Raby, GUT scale threshold corrections in a complete supersymmetric SO(10) model: Alpha-s (m(z)) versus proton lifetime, Phys. Rev. D **54**, 2261 (1996).
[26] A. Kusenko, Color, charge breaking minima in the MSSM, Nucl. Phys. A, Proc. Suppl. **52**, 67 (1997).
[27] U. Chattopadhyay and A. Dey, Exploring MSSM for charge and color breaking and other constraints in the context of Higgs@125 GeV, J. High Energy Phys. 11 (2014) 161.
[28] T. E. W. Group (CDF and D0 Collaborations), Combination of CDF and D0 results on the mass of the top quark, arXiv:0903.2503.
[29] I. Gogoladze, Q. Shafi, and C. S. Un, Higgs boson mass from t-b-τ Yukawa unification, J. High Energy Phys. 08 (2012) 028.
[30] M. A. Ajaib, I. Gogoladze, Q. Shafi, and C. S. Un, A predictive Yukawa unified SO(10) model: Higgs and sparticle masses, J. High Energy Phys. 07 (2013) 139.
[31] I. Gogoladze, R. Khalid, S. Raza, and Q. Shafi, Higgs and sparticle spectroscopy with Gauge-Yukawa unification, J. High Energy Phys. 06 (2011) 117.
[32] G. Belanger, F. Boudjema, A. Pukhov, and R. K. Singh, Constraining the MSSM with universal gaugino masses and implication for searches at the LHC, J. High Energy Phys. 11 (2009) 026.

[33] P. Bechtle, O. Brein, S. Heinemeyer, O. Stl, T. Stefaniak, G. Weiglein, and K. E. Williams, HiggsBounds-4: Improved tests of extended Higgs sectors against exclusion bounds from LEP, the Tevatron and the LHC, Eur. Phys. J. C **74**, 2693 (2014).
[34] P. Bechtle, S. Heinemeyer, O. Stl, T. Stefaniak, and G. Weiglein, HiggsSignals: Confronting arbitrary Higgs sectors with measurements at the Tevatron and the LHC, Eur. Phys. J. C **74**, 2711 (2014).
[35] R. Aaij *et al.* (LHCb Collaboration), First Evidence for the Decay $B_s^0 \to \mu^+\mu^-$, Phys. Rev. Lett. **110**, 021801 (2013).
[36] Y. Amhis *et al.* (Heavy Flavor Averaging Group Collaboration), Averages of B-hadron, C-hadron, and tau-lepton properties as of early 2012, arXiv:1207.1158.
[37] D. Asner *et al.* (Heavy Flavor Averaging Group Collaboration), Averages of b-hadron, c-hadron, and τ-lepton properties, arXiv:1010.1589.
[38] G. Blanger, F. Boudjema, A. Pukhov, and A. Semenov, MicrOMEGAs4.1: Two dark matter candidates, Comput. Phys. Commun. **192**, 322 (2015).
[39] E. Komatsu *et al.* (WMAP Collaboration), Seven-year Wilkinson microwave anisotropy probe (WMAP) observations: Cosmological interpretation, Astrophys. J. Suppl. Ser. **192**, 18 (2011).
[40] D. N. Spergel *et al.* (WMAP Collaboration), Wilkinson microwave anisotropy probe (WMAP) three year results: Implications for cosmology, Astrophys. J. Suppl. Ser. **170**, 377 (2007).
[41] S. Chatrchyan *et al.* (CMS Collaboration), Observation of a new boson at a mass of 125 GeV with the CMS experiment at the LHC, Phys. Lett. B **716**, 30 (2012).
[42] C. Patrignani *et al.* (Particle Data Group Collaboration), Review of particle physics, Chin. Phys. C **40**, 100001 (2016).
[43] P. A. R. Ade *et al.* (Planck Collaboration), Planck 2013 results. XVI. Cosmological parameters, Astron. Astrophys. **571**, A16 (2014).
[44] L. Calibbi, J. M. Lindert, T. Ota, and Y. Takanishi, Cornering light neutralino dark matter at the LHC, J. High Energy Phys. 10 (2013) 132.
[45] ATLAS Collaboration and T. A. Collaboration, Report No. ATLAS-CONF-2017-022.
[46] E. Aprile *et al.* (XENON Collaboration), First Dark Matter Search Results from the XENON1T Experiment, Phys. Rev. Lett. **119**, 181301 (2017).
[47] E. Aprile *et al.* (XENON Collaboration), Physics reach of the XENON1T dark matter experiment, J. Cosmol. Astropart. Phys. 04 (2016) 027.
[48] J. Aalbers *et al.* (DARWIN Collaboration), DARWIN: Towards the ultimate dark matter detector, J. Cosmol. Astropart. Phys. 11 (2016) 017.
[49] G. W. Bennett, B. Bousquet, H. N. Brown, G. Bunce, R. M. Carey, P. Cushman *et al.* (Muon g-2 Collaboration), Final report of the e821 muon anomalous magnetic moment measurement at bnl, Phys. Rev. D **73**, 072003 (2006).
[50] G. W. Bennett, B. Bousquet, H. N. Brown, G. Bunce, R. M. Carey, P. Cushman *et al.* (Muon g-2 Collaboration), Improved limit on the muon electric dipole moment, Phys. Rev. D **80**, 052008 (2009).
[51] J. Grange *et al.* (Muon g-2 Collaboration), Muon (g-2) technical design report, arXiv:1501.06858.
[52] N. Saito and J-PARC g-'2/EDM Collaboration, A Novel Precision Measurement of Muon g-2 and EDM at J-PARC, AIP Conf. Proc. **1467**, 45 (2012).
[53] M. Davier, A. Hoecker, B. Malaescu, and Z. Zhang, Reevaluation of the hadronic contributions to the muon g-2 and to alpha(MZ), Eur. Phys. J. C **71**, 1515 (2011).
[54] J. Y. Araz, M. Frank, and B. Fuks, Differentiating $U(1)'$ supersymmetric models with right sneutrino and neutralino dark matter, Phys. Rev. D **96**, 015017 (2017).
[55] A. M. Sirunyan *et al.* (CMS Collaboration), Search for dijet resonances in proton—proton collisions at $\sqrt{s} = 13$ TeV and constraints on dark matter and other models, Phys. Lett. B **769**, 520 (2017).
[56] M. Ackermann *et al.* (Fermi-LAT Collaboration), The Fermi galactic center GeV excess and implications for dark matter, Astrophys. J. **840**, 43 (2017).
[57] L. Accardo *et al.* (AMS Collaboration), High Statistics Measurement of the Positron Fraction in Primary Cosmic Rays of 0.5?500 GeV with the Alpha Magnetic Spectrometer on the International Space Station, Phys. Rev. Lett. **113**, 121101 (2014).
[58] V. Balkanov *et al.*, An upper limit on the diffuse flux of high energy neutrinos obtained with the Baikal detector NT-96, Astropart. Phys. **14**, 61 (2000).
[59] M. G. Aartsen *et al.* (IceCube Collaboration), Evidence for high-energy extraterrestrial neutrinos at the IceCube detector, Science **342**, 1242856 (2013).
[60] C. Degrande, C. Duhr, B. Fuks, D. Grellscheid, O. Mattelaer, and T. Reiter, UFO—The universal FeynRules output, Comput. Phys. Commun. **183**, 1201 (2012).
[61] J. Alwall, R. Frederix, S. Frixione, V. Hirschi, F. Maltoni, O. Mattelaer, H.-S. Shao, T. Stelzer, P. Torrielli, and M. Zaro, The automated computation of tree-level and next-to-leading order differential cross sections, and their matching to parton shower simulations, J. High Energy Phys. 07 (2014) 079.
[62] R. Abbasi *et al.* (IceCube Collaboration), The IceCube data acquisition system: Signal capture, digitization, and time-stamping, Nucl. Instrum. Methods Phys. Res., Sect. A **601**, 294 (2009).
[63] H. Baer, V. Barger, J. S. Gainer, P. Huang, M. Savoy, H. Serce, and X. Tata, What hadron collider is required to discover or falsify natural supersymmetry?, Phys. Lett. B **774**, 451 (2017).
[64] H. Baer, V. Barger, J. S. Gainer, P. Huang, M. Savoy, D. Sengupta, and X. Tata, Gluino reach and mass extraction at the LHC in radiatively-driven natural SUSY, Eur. Phys. J. C **77**, 499 (2017).